

Full-Scale Wind Tunnel Test of the UH-60A Airloads Rotor

Thomas R. Norman
National Aeronautics and Space Administration

Patrick Shinoda
Aeroflightdynamics Directorate (AMRDEC)
U.S. Army Research, Development, and Engineering Command

Randall L. Peterson
National Aeronautics and Space Administration

Anubhav Datta
Science and Technology Corporation
Ames Research Center, Moffett Field, CA

ABSTRACT

A full-scale wind tunnel test of the UH-60A airloads rotor was recently completed in the National Full-Scale Aerodynamics Complex 40- by 80-Foot Wind Tunnel. The rotor was the same one tested during the landmark 1993 NASA/Army UH-60A Airloads flight test and included a highly pressure-instrumented blade to measure rotor airloads. This paper provides an overview of the wind tunnel test, including detailed descriptions of the hardware, instrumentation, and data acquisition and reduction systems. In addition, the data validation process, the test objectives and approach, and some sample results are presented. The test has produced unique data not available from the flight test, including data from new measurements as well as data acquired at conditions outside the conventional flight envelope. The new measurements included rotor balance forces and moments, oscillatory hub loads, blade displacements and deformations, and rotor wake measurements using large-field Particle Image Velocimetry and Retro-reflective Background Oriented Schlieren. The new flight conditions included 1-g flight simulations up to advance ratios of 0.40, parametric sweeps at non-standard conditions, including multiple sweeps into stall, and slowed rotor simulations up to advance ratios of 1.0. These new data should provide an excellent resource for validating new and emerging predictive tools.

NOTATION

c	blade chord, in
C_L	rotor lift coefficient
C_P	rotor power coefficient
C_T	rotor thrust coefficient
C_X	rotor propulsive force coefficient
L/D_e	rotor lift divided by equivalent drag
M	local Mach number
$M^2 c_c$	section chord force
$M^2 c_m$	section pitching moment
$M^2 c_n$	section normal force
M_{tip}	hover tip Mach number
r	radial coordinate, ft
R	blade radius, ft
α_c	corrected shaft angle, positive aft, deg
α_s	geometric shaft angle, positive aft, deg
μ	advance ratio

ψ	rotor azimuth, deg (0 aft)
σ	rotor solidity
θ_0	collective pitch angle, deg

INTRODUCTION

Flight testing of the UH-60A airloads rotor in 1993 (Refs. 1, 2) resulted in a unique and extensive database for many level flight and transient maneuver conditions. The key data from this test were the rotor airloads (section normal force, pitching moment, and chord force) integrated from chordwise pressure arrays located at nine radial stations. These data, in combination with other measured parameters (structural loads, control positions, and rotor shaft moments), have helped to provide physical insights into specific flight regimes, including high speed flight (Ref. 3) and dynamic stall (Ref. 4), as well as providing critical data for validating new and emerging predictive tools (Refs. 5, 6).

Presented at the American Helicopter Society 67th Annual Forum, Virginia Beach, VA, May 3-5, 2011. This is a work of the U.S. government and is not subject to copyright protection in the U.S.

To provide an expanded database for validation of these predictive tools, NASA and the U.S. Army have recently

completed (May 2010) a full-scale wind tunnel test of the UH-60A airloads rotor, including the pressure-instrumented blade. This test, conducted in the USAF National Full-Scale Aerodynamics Complex (NFAC) 40- by 80-Foot Wind Tunnel, was designed to produce unique data not available from the flight test. This included data from a number of new measurements, such as rotor balance forces and moments, oscillatory hub loads, blade displacements and deformations, and rotor wake measurements using large-field Particle Image Velocimetry (PIV) and Retro-reflective Background Oriented Schlieren (RBOS). This also included data acquired at conditions outside the conventional flight envelope, such as at high speed, high thrust, and slowed-rotor conditions.

The primary wind tunnel test data were acquired during speed sweeps at 1-g simulated flight conditions, up to advance ratios of $\mu=0.4$, and during parametric thrust sweeps (up to and including stall) at various combinations of shaft angles and forward speeds. Data were also acquired at matching conditions from previous full-scale flight test and small-scale wind tunnel test (Ref. 7) to assess rotor and wind tunnel scaling issues. Finally, data were acquired while performing unique slowed-rotor simulations at reduced RPM (40% and 65%), up to advance ratios of $\mu=1.0$.

The objective of this paper is to provide an overview of this recently completed wind tunnel test. The paper includes detailed descriptions of the hardware, instrumentation, and data acquisition and reduction systems. In addition, the data validation process, the test objectives and approach, and some sample results are presented. Additional details on the slowed-rotor simulations as well as data comparisons with predictions can be found in Ref. 8 and 9, respectively.

DESCRIPTION OF THE EXPERIMENT

The test was conducted in the NFAC 40- by 80-Foot Wind Tunnel using a Sikorsky Aircraft UH-60A rotor system mounted on the NFAC Large Rotor Test Apparatus (LRTA). Figure 1 shows the model installed in the wind tunnel. In the following sections, detailed information is provided describing the experiment, including test hardware, instrumentation, data acquisition and reduction systems, pre-test activities, and rotor trim procedures.

Hardware

The wind tunnel, test stand, and all rotating hardware are described in the following section.

NFAC 40- by 80-Foot Wind Tunnel

The 40- by 80-Foot Wind Tunnel is part of the National Full-Scale Aerodynamics Complex (NFAC) located at NASA Ames Research Center. The NFAC, closed in 2003,

was reactivated by the U.S. Air Force under a long-term lease agreement with NASA and is managed and operated by the U.S. Air Force's Arnold Engineering Development Center (AEDC). The tunnel has a closed test section with semicircular sides, a closed-circuit air return passage, and is lined with sound-absorbing material to reduce acoustic reflections. The actual test section dimensions are 39 feet high, 79 feet wide, and 80 feet long and the maximum test section velocity is approximately 300 knots.



Figure 1. UH-60A Airloads rotor installed on LRTA in NFAC 40-by 80-Foot Wind Tunnel.

NFAC LRTA Test Stand

The LRTA (Fig. 1) is a special-purpose drive and support system designed to test helicopters and tilt rotors in the NFAC. Its primary design features include 1) a drive system powered by two 3000 HP motors, 2) a five-component rotor balance to measure steady and unsteady rotor hub loads, along with an instrumented flex-coupling to measure rotor torque and residual normal force, 3) a six-component fuselage load-cell system to measure steady fuselage loads, 4) a complete rotor control system with primary and dynamic actuator control, and 5) an output shaft assembly with a replaceable upper shaft to allow different rotor systems to be mounted. A detailed description of the LRTA and its capabilities can be found in Ref. 10.

Non-rotating swashplate control is provided through three identical actuator assemblies, each of which includes both primary and dynamic actuators. The primary actuators are high-authority/low-speed ball-screw electric actuators and are used to provide primary control of rotor blade pitch by raising/lowering and tilting the swashplate. The dynamic actuators are low-authority (± 2 deg of blade pitch for this test), high-speed rotary-hydraulic actuators and are used to provide time-varying perturbations to the swashplate. Each primary/dynamic actuator pair operates in series to provide the total swashplate actuation.

Control of the actuator assemblies is provided through two separate, and somewhat independent, position control systems, the Primary Control Console (PCC) and the Dynamic Control Console (DCC). The PCC provides the operator with low-bandwidth control of the three linear electric (primary) actuators. This position control is achieved by driving three stationary control rods, whose positions define the orientation of the swashplate; and, hence, rotor blade collective and cyclic pitch. The DCC provides the operator with control of the three rotary-hydraulic (dynamic) actuators to provide oscillatory pitch-angle perturbations about the nominal angle set by the PCC. Internal DCC capabilities allow control inputs to a single actuator or to any of the helicopter's control axes (collective, lateral or longitudinal). In addition to these internal capabilities, externally generated signals can be used to drive the actuators. For this test, the dynamic actuators were controlled with an external control system (designated the Trim Control System) through the DCC external inputs.

The LRTA was mounted on three struts as shown in Fig. 1, allowing for an angle-of-attack range of $+15^\circ$ to -15° . This installation put the rotor plane (at $\alpha_S=0$ deg) 10.9 inches above the tunnel centerline (20.4 ft above the acoustically treated floor).

Rotating Hardware

The rotating hardware used during this test was predominantly UH-60A flight hardware, with the exception of the instrumentation hat and a hydraulic collar assembly used on a previous full-scale test program (Ref. 11). A picture of this rotating hardware is shown in Fig. 2. The interface between the UH-60A rotor and LRTA occurred at three locations: the UH-60A shaft extender and the LRTA shaft, the swashplate guide and the LRTA upper unit, and the non-rotating swashplate and the LRTA stationary pushrods. Details of the rotor hardware and instrumentation hat are presented below.



Figure 2. Close-up of UH-60A rotating hardware.

The UH-60A is a four-bladed, articulated rotor system consisting of four subsystems: hub, blade pitch controls, bifilar vibration absorber, and main rotor blades. The four titanium-spar main rotor blades attach to spindles that are retained (by elastomeric bearings) to a one-piece titanium hub. These bearings permit blade flapwise and lead-lag motion. Main rotor dampers are installed between each of the main rotor spindles and the hub to restrain lead-lag motion of the main rotor blades during rotation and to absorb rotor head starting loads. Blade pitch is controlled through adjustable pitch links that are moved by the swashplate. A bifilar vibration absorber is typically mounted on top of the hub to reduce rotor vibration. For this test, the bifilar four-arm plate was installed but the bifilar weights were not attached.

The blades used in this test program were the same 4 rotor blades flown during the UH-60A Airloads Program (Ref. 1). Two of these blades were heavily instrumented by Sikorsky Aircraft under NASA contract: one with 242 pressure transducers and one with a mix of strain-gages and accelerometers. Details of the rotor blade instrumentation are provided in a later section. A summary of relevant main rotor system parameters is presented in Table 1 and Ref. 12. A summary of the blade dynamic characteristics can be found in Ref. 13.

Table 1. UH-60A Rotor Parameters

Parameter	Value
Number of blades	4
Radius, ft	26.83
Nominal chord, in	20.76
Equivalent blade twist, deg	-18
Blade tip sweep, deg aft	20
Geometric solidity ratio	.0826
Airfoil section designation	SC1095/SC1095R8
Nominal thickness, % chord	9.5
100% RPM	258

The instrumentation hat, mounted on top of the UH-60A hub, provided a location for terminating instrumentation wiring and mounting the Rotor Mounted Data Acquisition and Transmission System (RMDATS). Details of the RMDATS are provided in the Data Acquisition Systems section below. An aerodynamic fairing was designed to protect these components as well as minimize undesirable aerodynamic forces. To reduce uncertainties when comparing with flight test data, the fairing was designed to duplicate, as closely as possible, the instrumentation fairing used during the UH-60A Airloads flight test.

Instrumentation

A total of 332 rotor and hub parameters (Table 2) and 124 LRTA and wind tunnel parameters (Table 3) were measured and acquired as part of this test program. The following

section briefly describes the key measurements from these parameter groups, including select calibration procedures where appropriate. Other independent instrumentation and measurement systems are described in a later section.

Table 2. Rotor Instrumentation

Measurement Type	Number of gages
Blade pressures	235
Blade bending moments	28
Pitch, flap and lag angles	24
Shaft moment, shaft stress, hub arm vertical shear	12
Pitch link, damper and rotating scissor loads	12
Miscellaneous spindle and blade stresses	18
Hub accelerometers	3

Table 3. LRTA and Wind Tunnel Instrumentation

Measurement Type	Number of gages
Balance and flex-coupling forces and moments	28
Balance and flex-coupling temps	16
Stationary pushrods, scissors and swashplate guide (forces/moments)	8
Control system positions/commands	15
Fuselage loadcells	6
Tunnel pressures and temperatures	31
Model angles and RPM	4
Data Transfer Computer and trim controller parameters	16

UH-60A Rotor Blade and Hub Instrumentation

Blade Pressures. As discussed in Ref. 1 and 14, the pressure blade was originally built with 242 sub-miniature pipette-type absolute pressure transducers embedded below the skin surface of the blade. The majority of transducers were located in one of nine chordwise arrays, with the remainder located near the blade leading edge to better determine blade vortex interaction locations. The layout of the transducers is shown in Fig. 3. The chordwise Gaussian spacing of the transducers was selected to allow for accurate, integrated measurements of the radial airloads. During the flight test program, a number of these transducers and/or their wiring failed. Prior to the wind tunnel test, the failed transducers were replaced or the wiring modified so that 235 of the pressure transducers were operational. After the first set of hover and forward flight runs, 20 of these transducers became suspect, leaving a total of 215 working transducers at the beginning of forward flight research testing.

Calibrations of the pressure transducers were performed using the in-blade calibration technique developed for the

flight test program (Ref. 1). A mylar sleeve was placed over the blade and both ends sealed with a flexible sealing compound. Near the root the sleeve is sealed against the airfoil section and near the tip the sleeve is sealed against itself forming an airtight chamber. Between the blade and sleeve was a breather cloth to allow the free flow of air along the length of the blade and to prevent the mylar from sealing off any of the pressure transducers. A vacuum pump and control unit was then attached to the sleeve and air was removed from the sealed sleeve to create a uniform pressure field around the blade down to 8 psi. Data were collected through the RMDATS to determine the calibration coefficients. Three separate calibrations were performed, one in the laboratory prior to testing and two in the wind tunnel. Since the differences between calibrations were minimal, the coefficients determined from the laboratory calibrations were used for all subsequent data reduction.

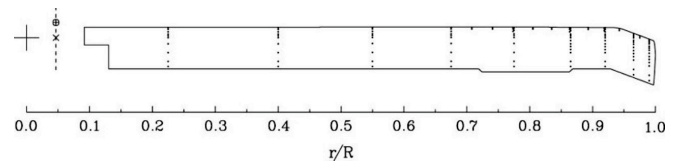


Figure 3. Location of pressure transducers on pressure-instrumented blade.

Blade Bending Moments. Blade normal, edgewise, and torsional moments were measured with a total of 26 two- or four-leg strain-gage bridges bonded to the second instrumented blade. The gages were located at the blade root (11.3% radius) and then evenly distributed along the blade at 10% increments of the rotor radius (20% to 90%). Twenty-one of these gages were bonded directly to the blade spar and used during the Airloads flight test. Five additional torsion gages were bonded to the blade skin, including one at the same radial station as a spar-bonded gage to ensure measurement consistency. In addition, two blade bending measurements were acquired at the root of the pressure blade as back-ups.

The blades were calibrated statically prior to testing. Separate calibrations were performed for normal, edgewise, and torsional moments and corrections were made for the blade twist distribution in the applied loading. Gage cross-coupling effects were accounted for in the calibration although, for most test conditions, these effects were small.

Blade Root Motion Measurements. The hub instrumentation also included two independent, specially-designed blade motion measurement systems used to determine blade flap, lag, and pitch angles at the root of each blade. These systems were required because the UH-60A elastomeric bearing configuration does not allow direct measurement of blade root motion (pitch, flap, lag) with displacement or angular measurements. The first system, designated the Blade Motion Hardware (BMH) system, was

used during the Airloads flight test (Ref. 1). The BMH (Fig. 4) are mechanical measurement devices that span the main-rotor blade hinge points, and include three Rotary Variable Differential Transformers (RVDTs) on each blade to measure the relative motions of its own articulations. The true blade motions are obtained through three kinematic equations that account for the cross-coupling between measurements.



Figure 4. Blade Motion Hardware mounted on UH-60A hub.

The second system, designated the Rotor State Measurement System, was first developed and used during testing of the U.S. Army RASCAL aircraft (Ref. 15). This system is composed of four sets of three laser distance transducers (one set mounted to each hub arm). Each transducer produces a laser beam that is reflected back to a sensor in the same enclosure by reflective objects within a specified distance range. The transducer then produces a voltage proportional to the distance to the object (and related to one of the blade root angles). The transducers and reflective objects are positioned to minimize the cross-coupling between measurements.

The calibration of both systems was performed simultaneously in the wind tunnel. Each blade was moved relative to the hub over a specified range of flap, lag and pitch angles. BMH and laser sensor measurements were acquired at each position while also measuring the blade angular position with respect to the hub using inclinometers and a surveying transit. Non-linear regression analyses were then performed with the collected data to calculate appropriate calibration coefficients.

Rotating hub load measurements. The rotor shaft was instrumented with four strain gages to measure shaft stress and four strain-gage bridges to measure shaft moment. Two of the shaft moment bridges were positioned 90 deg apart on the UH-60A shaft extender and two were positioned 90 deg

apart further down on the LRTA shaft. This positioning allowed for the calculation of rotating shear forces and moments centered at the rotor hub. The shaft extender moment gages were calibrated at Sikorsky Aircraft's calibration laboratory using their transmission test stand. The LRTA shaft moment gages were calibrated at Ames Research Center prior to installation of the LRTA in the wind tunnel.

In addition, each rotor hub arm was instrumented with a strain-gage bridge to measure hub arm vertical shear force. These gages were calibrated with the LRTA installed in the wind tunnel. By combining these four shear measurements, another estimate of rotating hub moments could be determined, as well as an estimate of hub vertical force.

Other Rotating Parameters. The four pitch links, four dampers and two rotating scissors were instrumented with four-leg strain-gage bridges to measure the appropriate loads. Eighteen additional gages were installed on the spindles and blades to provide stress measurements for safety purposes. Finally, three orthogonal accelerometers were mounted inside the instrumentation hat at the center of rotation to measure hub vibration.

LRTA and Wind Tunnel Instrumentation

As discussed in Ref. 10, a five-component rotor balance with steady and dynamic load measuring capability is integrated into the LRTA. The four balance flexures are instrumented with 12 primary gages and 12 back-up gages which are combined to determine rotor normal, axial and side forces, together with the rotor pitching and rolling moments. In addition, 14 balance thermocouples are installed to measure balance temperature uniformity. The rotor shaft has an in-line flex-coupling, which is instrumented to redundantly measure rotor torque, residual power-train normal force, and temperature. All of these measurements were conditioned and acquired during this test. The original static calibration of the rotor balance is described in detail in Ref. 10. A new calibration was performed prior to this test with the resultant calibration coefficients being consistent with those from the original calibration.

A total of 8 strain-gage bridges were installed on the stationary control hardware to measure control system forces and moments, including three bridges on the stationary pushrods, one on the stationary scissors, and four on the swashplate guide. Two displacement measurements for each primary actuator and two displacement and one command measurement for each dynamic actuator (for a total of 15 measurements) were also acquired. The actuator displacement measurements were used to provide an alternative to the blade root motion measurements in determining collective, lateral cyclic, and longitudinal cyclic pitch.

Six load cells were installed between the LRTA aerodynamic fairing and the fixed LRTA chassis. These measurements were combined to provide steady fuselage loads (lift, drag, side, pitch, roll, and yaw).

The wind tunnel instrumentation included 31 pressures and temperatures used to derive tunnel and model operating conditions. In addition, 3 model angles and rotor RPM (derived from the 4096/rev phototach) were measured.

Data Acquisition Systems

Six separate systems were used during this test program to provide signal conditioning and/or digitize, reduce, and store data. The two primary systems were the NFAC Data Acquisition System (NFAC DAS) and the RMDATS. These two systems provided signal conditioning for the primary research data (pressures, strain gages, etc.) and then digitized and stored the time history data at the specified rate. Four auxiliary systems were also utilized, including the Data Transfer Computer (DTC), the Trim Control System, the LRTA Rotor Control Console, and the Fatigue Monitoring System. A short description of each system is provided in the following sections.

NFAC DAS

The NFAC DAS was the primary data acquisition system for the low-speed channels (data acquired at 256/rev). It was developed by the Air Force to provide 16-bit digitization and storage capabilities for tests conducted in the NFAC (Ref. 16). Key features include a large available channel count, variable sample rates based on the rotor N/rev, and variable data record lengths, up to 256 revolutions. In addition, the system allows multiple data points to be recorded consecutively, effectively increasing the amount of time that continuous data can be recorded. The NFAC DAS uses an oversample/re-sample technique to ensure all data are aligned with the rotor azimuth position. Corrections for any time delay caused by the NFAC anti-aliasing filters are incorporated during the re-sample process. The filters were set to 400 Hz for the majority of this test, and 200 Hz for low RPM testing. The trigger signal for data acquisition was generated by an optical encoder mounted on the model, with the $\psi=0$ deg reference position defined when the pressure blade points downstream (the same reference as used during the flight test). Data were sampled at a rate of 256 samples/rev and for a range of sample durations, ranging from 16 to 256 revolutions, depending on the specific test objective. For select test conditions, the multiple point capability was used to record up to 180 seconds of continuous data, split into three 256-revolution data points. In addition to this data acquisition function, the NFAC DAS also provided both real-time and post-point data reduction and processing capabilities.

RMDATS

The RMDATS was the primary data acquisition system for the high-speed blade pressure channels (data acquired at 2048/rev). This rotor-mounted system was developed by Accumetrics Associates, under NASA contract, specifically for this test program. The rotating data system was necessary because the capabilities of the existing analog systems (including the analog slipring) were insufficient to handle the large number of channels.

The primary function of the RMDATS is to provide signal conditioning for up to 256 channels, digitize the data (16-bit), and transmit it from the rotor head to a ground station at speeds up to 10KHz per channel (for a maximum aggregate rate of 3MHz). The design of RMDATS consists of three subsystems: the Rotating Subsystem, the Transmission Subsystem and the Ground Subsystem. The Rotating Subsystem (Fig. 5) is designed to be located inside the rotor model's instrumentation hat and can continuously condition and simultaneously digitize 256 resistive-bridge sensors (typically pressure transducers or strain gages). Key features include variable filter and gain settings, auto-zero and shunt functions, as well as variable sample rates based on the rotor N/rev. The resulting data is combined into sixteen digital data streams each representing sixteen of the sensors along with associated status information. These streams are modulated so that they may be transmitted off the rotor by a non-contact method.



Figure 5. Rotating Subsystem of Rotor Mounted Data Acquisition and Transmission System (RMDATS).

The Transmission Subsystem, located near the bottom of the LRTA includes mechanical sliprings and a capacitive data coupler. The mechanical sliprings are used only to transmit power to the rotor and to handle low speed digital communications for control and monitoring functions. The capacitive data coupler provides a non-contact means (with minimal noise) of transmitting multiple streams of high-speed digital data from the rotor as well as transmitting

azimuth information derived from the optical encoder to the rotor.

The Ground Subsystem consists of a rack of receivers that recovers the data transmitted from the rotor and communicates all data along with status and channel identification information via an Ethernet-based computer network to a PC-based workstation. This subsystem supplies data display, analysis and storage capabilities. The Ground System also provides the user interface for control and monitoring of the system's functions.

For this test, the RMDATS was configured to digitize data at 2048/rev with the data acquisition synchronized with the NFAC DAS. The anti-aliasing filters were set to 2000 Hz for the majority of the test, and 1000 Hz for low RPM testing. Corrections for any time delay caused by these filters were incorporated during post processing.

Auxiliary Data Systems

The following four auxiliary data systems were used to enable safe and efficient operation of the test.

Data Transfer Computer. The Data Transfer Computer (DTC) was designed to acquire analog data, compute derived parameters, and provide the derived data in analog form to the Trim Control System in near real-time. All analog input data were provided through the NFAC DAS amplifiers, sent through 100 Hz anti-aliasing filters, and digitized at 256 samples/rev. These data were simultaneously sampled, converted to engineering units, combined together into the desired derived parameters, and then converted to analog output with a total delay of one-half the sampling period. These analog data were then sent to the Trim Control System as well as to the NFAC DAS for acquisition and storage. The derived data included hub-axis forces and moments derived from both the rotor balance and the shaft bending gages as well as rotor 1/rev flapping.

Trim Control System. In addition to its primary task of controlling the LRTA dynamic actuators for trim control, the Trim Control System was designed to provide data acquisition, reduction, and analysis capabilities. Analog input data from the DTC were sent through a 100 Hz anti-aliasing filter before being digitized by the Trim Control System. Recorded data included all input and output voltage and engineering unit channels, and internal trim control parameters used for development and validation of the controller. Data records for each test point were extracted in post-run data processing. Analog outputs of many of the system parameters, including actuator commands, were also provided to the NFAC DAS for final digitization and storage.

LRTA Rotor Control Console. The LRTA Rotor Control Console provided the primary signal conditioning for both primary and dynamic LRTA actuator positions. In addition, the console provided the primary signal conditioning for two of the four BMH flap RVDTs as well as two of the four BMH pitch RVDTs. Anti-aliasing filters were set to 500 Hz for all blade gages. Analog outputs of all these measurements, in addition to dynamic actuator command positions, were provided to the NFAC DAS for final digitization and storage.

Fatigue Monitoring System. To meet the test objectives of this program, it was necessary to monitor the accumulation of fatigue damage on various rotor and LRTA components. An on-line Fatigue Monitoring System was developed to accomplish this task. This system was designed to measure, calculate and display the magnitude of each fatigue-critical parameter for each rotor revolution, in real time. The developed system was capable of recording up to 32 input measurements; derived parameters could be calculated from any of these inputs. The rotor 1/rev signal triggered acquisition of data samples equally spaced about the azimuth. The oscillatory load was then calculated from the maximum and minimum values measured during the current rotor revolution, compared to the endurance limit for each parameter, and recorded if the endurance limit was exceeded.

Independent Measurement Systems

In addition to the instrumentation and data systems mentioned above, three independent image-based measurement systems were used during this test to provide unique research data. They included the Blade Displacement system, the Retro-reflective Background Oriented Schlieren system and the large-field Particle Image Velocimetry system.

Blade Displacement

The goal of the Blade Displacement system was to measure the displacements and deformations of all four rotor blades as they rotated through the four rotor quadrants. From these measurements, it is possible to determine the blade root pitch, flap, and lag, as well as the dynamic deformations of the flexible rotor blades, to compare with other measurements and with predictions.

The blade displacement measurements were made with a multi-camera photogrammetry system developed during two preceding rotor tests (Ref. 17). The final system consisted of four PCs with frame grabber boards, eight 4-Mega-pixel 12-bit CCD progressive scan digital cameras, 16 high-power xenon flash-lamp strobes, and specialized image acquisition software. The cameras and strobes were installed in the test section floor cavities, with a pair of cameras nominally

viewing each quadrant of the 360-degree rotor azimuth (Fig. 6). The actual view of a given camera was not limited to a single rotor quadrant, however, allowing 3 and 4-camera photogrammetric intersections because of the overlapping camera views. Fiber optic bundles that route the light from each strobe were positioned as close as possible to the optical axes of the lenses in order to maximize the light return from retro-reflective targets attached to the lower surface of each rotor blade. A total of 48 retro-reflective targets were used per blade, three targets per radial station, uniformly spaced (5% of the radius) between the blade cuff and blade tip (Fig. 7). A detailed description of the final system design and installation is provided in Ref. 18.

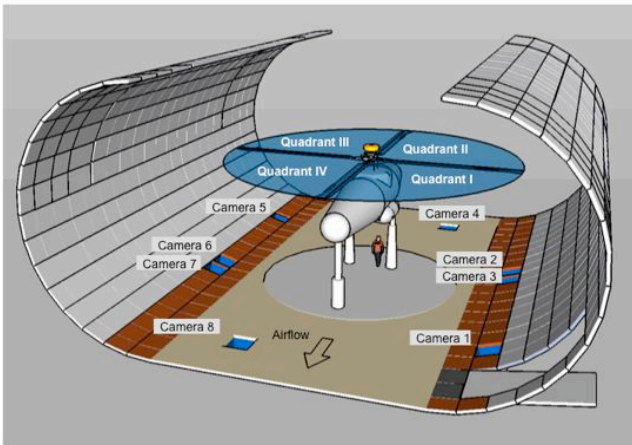


Figure 6. Test section schematic identifying Blade Displacement camera floor cavities and rotor quadrants.

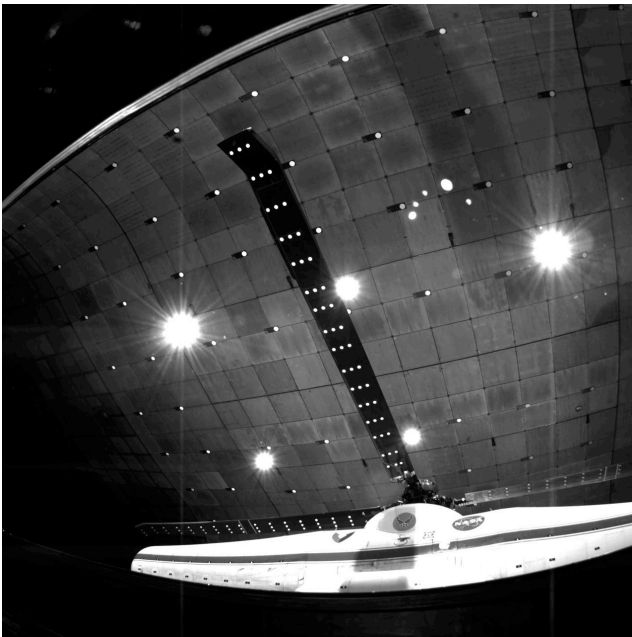


Figure 7. Rotor blades mounted on LRTA in NFAC test section showing Blade Displacement 2-inch diameter retro-reflective targets.

During data acquisition, all eight cameras were synchronized with the rotor 1/rev, producing one image set at a specific rotor azimuth. Multiple image sets were then acquired at this azimuth to improve the precision of the ensemble averages. Image sets were then acquired at multiple rotor azimuth locations in order to adequately capture the displacements of all the blades in each of the four rotor quadrants. The most highly documented test conditions consisted of 60 revolutions of data per azimuth for 8 cameras at 40 rotor azimuth locations, producing 19,200 individual images. This required a total data acquisition time of approximately 10 minutes per test condition.

Specialized photogrammetry software is currently being developed to extract the rotor blade displacement data from the thousands of images for each test condition. This effort is progressing well and initial results are promising. Sample results for one of the 27 most highly documented test conditions are shown in Figs. 8 and 9. Figure 8 shows the average vertical displacement of each blade as a function of rotor azimuth at two different radial stations, one near the root and one near the tip.

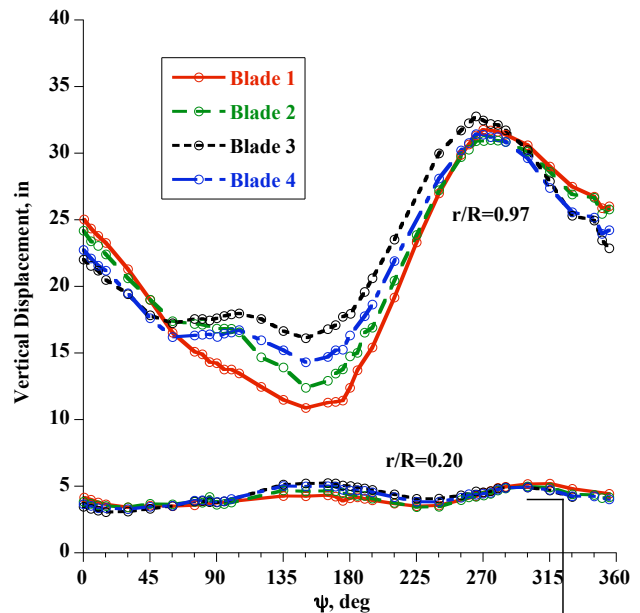


Figure 8. Vertical blade displacement data at two radial stations, $r/R=0.20$ and 0.97 , $C_T/\sigma=0.10$, $\alpha_s=0$ deg, $M_{tip}=0.650$, $\mu=0.30$.

Of note are the significant azimuthal variations at the tip caused by blade structural deformations as well as the differences between blades on the advancing side. Figure 9 shows the average vertical displacement for each blade as a function of blade radius for a single azimuth angle of 135 deg. For this plot, the displacements due to rigid flapping have been removed, leaving only the structural deformations of each blade as a function of radius. Of note is the similarity

of blade deformations relative to the root even though the absolute vertical displacements at the tip are different. This type of data is expected to be extremely valuable when validating the aerodynamic/structural coupling in our computational models.

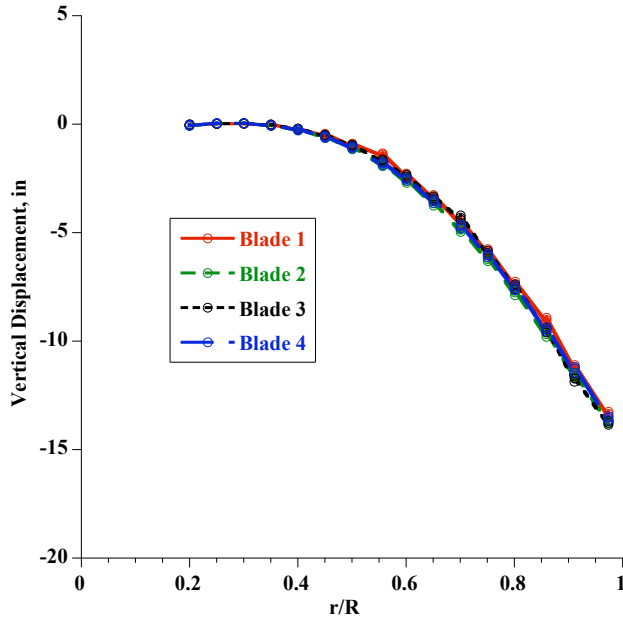


Figure 9. Vertical blade displacement data (rigid flapping removed) at $\psi=135$ deg, $C_T/\sigma=0.10$, $\alpha_s=0$ deg, $M_{tip}=0.650$, $\mu=0.30$.

Retro-reflective Background Oriented Schlieren (RBOS)

The goal of the RBOS system was to determine the location and extent of the rotor tip vortex filaments as they pass through an area on the advancing side of the rotor. This information (particularly the filament orientation as it passes through the PIV laser light sheet) will ultimately be combined with the PIV measurements to provide a better understanding of the rotor wake.

Background Oriented Schlieren (BOS) is an imaging technique that traces density gradients in transparent media (Ref. 19, 20). Similar to schlieren and shadowgraphy, BOS detects the deflections of light rays caused by refractive index changes due to the density gradient, but is used in situations where mirror or focusing schlieren methods are impractical. BOS requires only a digital camera, light source and speckle background. The background is imaged in both quiescent wind-off and wind-on test conditions. When a density gradient, such as a tip vortex, a sonic shock, or heat plume, lies between the speckled background and the camera, the locations of the speckles appear to shift towards the decreasing density. This apparent shift can then be measured by image cross correlation of the wind-on and wind-off images. Density can then be derived from the shift

using the Gladstone-Dale equation. In retro-reflective background oriented schlieren (RBOS), retro-reflective materials are used to increase the efficiency of the lighting and the contrast between the speckle and the background, thereby increasing the signal-to-noise ratio and allowing shorter integration times that can freeze unsteadiness in the flow. A detailed description of the RBOS technique and its first application to a rotor in the NFAC can be found in Ref. 21.

During the current test, RBOS was used to simultaneously image from two directions a region of interest (ROI) just downstream of the advancing blade to capture density gradients created by vortices shed by the blade (Ref. 21, 22). One camera viewed the ROI through a periscope mounted in a light fixture in the ceiling of the test section; the second camera was located in an existing window above the rotor plane and on the opposite side of the test section as the ROI (Fig. 10). The cameras were synchronized with the rotor 1/rev so that images were acquired over a range of blade azimuth positions. Vortices were evident in the wind-on images from both cameras as small image-plane displacements of the background speckle pattern toward the vortex core. An example image from one of the cameras is shown in Fig. 11. Correspondence of points on the vortices in the images of both cameras can then be established by enforcing epipolar geometry. The vortex coordinates/locations relative to the blade are then calculated from the image-plane coordinates using stereo photogrammetry.

RBOS images were acquired for most test conditions and data reduction is currently underway. Initial results are promising and suggest correlation with the PIV data will provide excellent results.

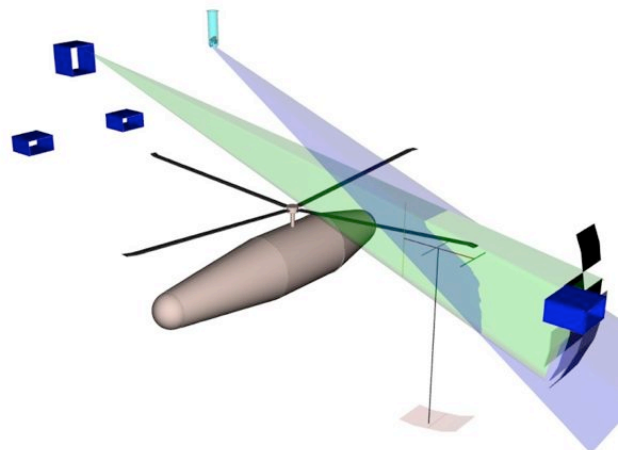


Figure 10. Test section schematic showing layout of RBOS system. Field of view from periscope camera shown in light blue; side-wall camera, green. Existing tunnel windows shown in navy, RBOS panels in black. Calibration mast is shown spanning field of view.

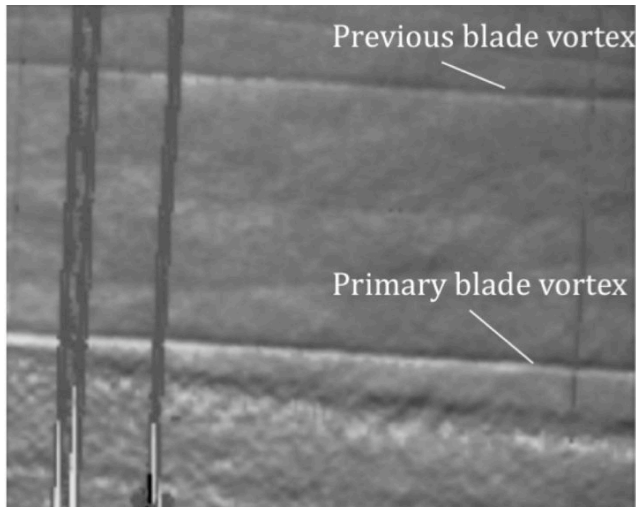


Figure 11. Sample RBOS image-plane displacement data. Vortices are visible as light and dark bands. Free-stream flow from left to right.

Particle Image Velocimetry (PIV)

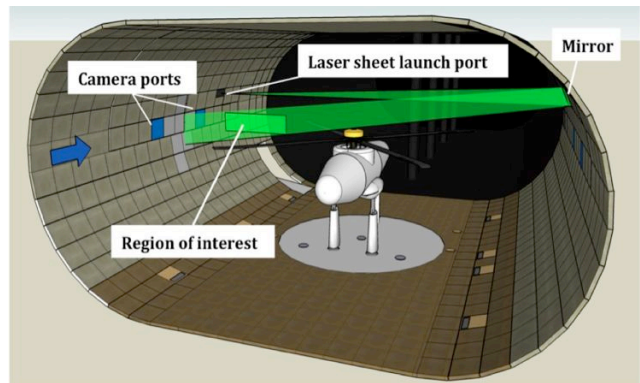
The goal of the PIV system was to measure the three-component velocity field in a stationary cross-flow plane over a large extent of the rotor-blade near-wake region. From these measurements it is possible to extract additional flow field information, including tip vortex core size, strength, and structure as well as the local tip vortex trajectories.

PIV is a well-regarded optical technique used to measure instantaneous three-component velocities in a plane. High-speed cameras are used to image seed particles illuminated by a laser sheet. The application of this technique to large ROI's can often present difficult design challenges. This was especially true for this test, with a desired ROI of 3.5-ft high and 14-ft wide, the largest ever attempted in the NFAC. Ultimately, the PIV system design was driven by the constraints imposed by the 40- by 80-Foot Wind Tunnel test section geometry and facility infrastructure. The test section ceiling and walls have a 4-ft thick acoustic lining with an outer steel shell, and the only optical access is via a limited number of facility camera ports. For this reason, some modifications to the facility were necessary. For example, a new optical port was installed to house a large-format mirror used to position the laser sheet in the desired streamwise location.

Even with these modifications, the PIV measurement plane was restricted to a single location. After careful consideration, the plane was positioned at approximately 90 deg rotor azimuth. This location was expected to provide the most useful data for understanding the evolution of the rotor wake and was the location preferred by key members of the CFD community. The optimal vertical location for the PIV

plane was determined computationally. CAMRAD II (Ref. 23) calculations were performed for a series of rotor test conditions. The intersections of the calculated tip vortex trajectory and trailed vortex sheet with the PIV plane at 90 deg rotor azimuth were determined, enabling a judicious selection of the plane height.

A detailed description of the final PIV system design and installation is provided in Ref. 24. The primary system components included: two TSI 11 Mp cameras with 120mm lens; a Spectra-Physics PIV laser, ~260 mJ per pulse @ 532 nm wavelength; four MDG seeders emitting 0.75 micron particles; a remotely-controlled (2 axes) mirror (36 in x 12 in, H x W); a 4-ft x 8-ft dual plane calibration plate; and the software INSIGHT 3G™ by TSI, Inc. Figure 12a shows a schematic of the PIV system installed in the tunnel. Figure 12b shows the path of the laser sheet in the test section during operation. During data acquisition, the laser and camera systems were synchronized with the rotor 1/rev so that measurements were acquired for different rotor blade azimuths relative to the laser light sheet. In general, 100 PIV frames were acquired for each blade position relative to the laser sheet.



a) Schematic



b) Actual installation

Figure 12. Test section schematic and photo showing PIV installation.

PIV measurements were acquired at a limited number of forward flight conditions. Data reduction is currently underway and initial results look very promising. Sample results are provided in a later section of this paper.

Data Reduction

The raw time history data acquired with the NFAC DAS and RMDATS (in volts and counts) were transferred post-run to NASA's Rotor Data Management System (RDMS) database for final storage. These data were subsequently corrected for filter effects (where necessary), converted to engineering units using appropriate calibration methods, and stored in the database.

In addition to providing database storage, the RDMS provided post-processing capabilities. For this test program, over 650 interim and final derived parameters were calculated for every data point acquired. Examples of derived data include tunnel velocity, rotor balance and fuselage forces and moments, blade root angles, rotor control positions, and rotating hub loads. These derived data also include non-dimensional parameters, including rotor coefficients for thrust and power, advance ratio, and tip Mach number.

One of the derived parameters, a wind tunnel wall correction (in the form of an induced angle correction) was calculated using the standard Prandtl-Glauert equations (Ref. 25). This correction term was used to correct the geometric shaft angle, and ultimately the rotor lift and propulsive force.

As was done for the Airloads flight test program, the blade absolute pressures were integrated to provide normal force, pitching moment, and chord force at up to nine radial stations. The same integration algorithm was used for both tests and included the use of mapped coordinates and 2nd order integration methods. The validity of these integrations is ultimately dependent on the location and number of working transducers in a given chordwise array. For the blade airloads presented in this paper, care was taken to ensure only working transducers were included in the integrations.

Pretest Activities

Prior to blades-on research testing, a number of pretest activities were performed, including shake testing, tare data acquisition, and rotor track and balancing. This section provides details of these activities.

Shake Testing

A shake test of the LRTA was conducted in the 40- by 80-Foot Wind Tunnel prior to wind-on testing to help evaluate the dynamic characteristics of the rotor balance. Rotor

balance, accelerometer, and shaft gage response data were acquired for lateral, longitudinal, vertical, and off-axis inputs at the hub. Data were also acquired to evaluate the effects of hub mass and model angle-of-attack. Analysis of these data has recently begun with the goal of providing a dynamic calibration matrix for the rotor balance. Ultimately, corrected hub loads from the rotor balance will be compared to hub loads derived from the rotor shaft and hub arm measurements.

Tares

Tare data were acquired to compensate for gravity effects as well as hub/shaft/control system aerodynamic loads and interference. The effects of gravity, or weight tare, were determined by acquiring mean rotor balance, fuselage load cell, shaft moment, and hub arm vertical shear data as a function of model angle-of-attack, both with and without rotor blades installed. The effects of hub/shaft/control system aerodynamics were determined by acquiring mean wind-on data without the rotor blades installed. These aerodynamic tare data were acquired with hub rotation over the complete range of tunnel speeds and model angles tested. The resultant data were analyzed to provide smooth analytical functions related to model angle-of-attack and wind tunnel dynamic pressure. Specific weight and aerodynamic tare values were ultimately calculated on a point-by-point basis and subtracted from the acquired data to isolate the measurements of interest.

Track and Balance

Rotor track and balance procedures were performed prior to the first research run. The rotor was first tracked in hover by adjusting pitch link lengths so that all four blades flew in the same plane (± 0.5 blade-tip thickness as seen through the tracking camera located at an azimuth angle of approximately 240 deg). Weights were then applied at the hub to minimize the 1/rev shear force as measured by the rotor balance. The track and balance were then checked at 40, 80, and 120 knots and no significant changes were observed. Note that no changes were made to the trim tab angles as part of the tracking procedure. Post-test analysis showed an increase in 1/rev normal force with airspeed that suggests a mild advancing-side out-of-track condition at higher speeds that was not apparent from the retreating-side tracking camera during the test.

Rotor Control Systems and Trim Procedures

This section describes the rotor control systems and the procedures to trim the rotor during testing.

Rotor Control Systems

Two separate rotor control systems were utilized during this test program, with each system controlling an independent set of actuators.

Control of the primary actuators was provided through the LRTA PCC, discussed above and in Ref. 10. The PCC provided low-bandwidth control of the three electric (primary) actuators and allowed the operator to manually trim the rotor based on displays of rotor force and moment coefficients, and rotor flapping. Due to the manual nature of this control system, achieving precise rotor trim conditions was sometimes difficult.

Control of the dynamic actuators was provided through the Trim Control System. This system provided closed-loop low-frequency (less than 2 Hz) control of the three hydraulic (dynamic) actuators in order to set the rotor trim state more precisely and quickly than was possible with manual control through the PCC. This system had the added benefit of being able to maintain the desired trim condition through long-period transients in wind tunnel flow. More detailed descriptions of the controller design and operation can be found in Refs. 11 and 26.

The trim controller was designed to continuously control up to three trim parameters through collective, longitudinal cyclic, and lateral cyclic pitch commands to the dynamic actuators. Parameters available for control during this test included rotor thrust or lift, hub pitching and rolling moment (from the LRTA balance), hub pitching and rolling moment (from a moment gage on the UH-60A shaft extender), and lateral and longitudinal flapping (from the BMH flapping RVDT on the pressure blade). Either dimensional or non-dimensional parameters could be specified. In addition, the rotor propulsive force could be set through manual changes to the model shaft angle. The trim controller calculated the shaft angle change required to obtain the desired propulsive force based on a look-up table of the propulsive force sensitivity to shaft angle change. Typically one or two shaft angle change iterations were required to converge on the desired rotor propulsive force.

Rotor Trim Procedures

The procedure to trim the rotor system during this test was to first have the rotor operator get close to the desired condition through manual control of the LRTA primary actuators. Precise force and moment trim values were then entered into the trim controller operator interface and the trim controller was activated in 'continuous' mode to drive the dynamic actuators to reach the desired condition. The trim controller continually updated the swashplate commands to maintain the desired trim condition throughout the duration of the data point.

As mentioned above, trimming to propulsive force required changes to the model shaft angle. These changes were calculated by the trim controller and called out to the LRTA model operator, who entered the shaft angle change manually. During this shaft angle change, the trim controller remained in 'continuous' mode to hold the other trim parameters (typically rotor lift and hub pitch and roll moments) at the desired values.

DATA VALIDATION

A number of approaches to validate the acquired data were used before, during, and after the test program. Descriptions of these approaches are provided in this section, along with a few examples. The current validation status for some of the key parameters is also provided.

Data Validation Approach

The validation approaches can be divided into three categories: instrumentation checks, internal consistency checks (comparing one type of measurement with another), and external consistency checks (comparing results with predictions or other experiments). Brief descriptions of these approaches are provided below.

The instrumentation checks included a number of pretest procedures to verify the identity of individual gages, to calculate voltage drops due to line length, and to check for amplifier drift. During each run, a number of reference points were acquired (zero, cal, hover, forward flight) to allow checks for consistency during runs as well as repeatability between runs. Finally, post-test evaluations of individual channels were performed to look for signal saturation and breakup, frequency response issues, and general unexpected behavior. Twice during the test, a complete RPM sweep was performed in hover at low collective. The data from these runs will be used to help assess whether any gage measurements were adversely affected by centrifugal (CF) loading.

The internal consistency checks consisted of four different types of comparisons. The first was comparison of measurements that have redundant gages located on the same hardware, such as the rotor balance or the blade root measurements. The second was comparison of similar measurements made on different hardware or with different methods, such as pitch link, damper, and blade root bending loads. The third was comparison of measurements related to one another but not measuring exactly the same thing, such as blade pressures at different chordwise stations. This latter type of comparison, in conjunction with the instrumentation checks, provided the best means for identifying faulty blade pressure channels. The final type was comparison of different revolutions of the same measurement to check for repeatability and steadiness during a data point. For steady,

forward-flight testing, these different revolutions should ideally show little variation.

The external consistency checks consisted of two types of comparisons, those with previous experiments and those with predictions. The most important comparisons are those between the wind tunnel test and the Airloads flight test. Because the hardware and instrumentation were mostly identical for these tests, comparisons of data at similar conditions can be used to identify discrepancies and ultimately determine if data acquired in one or the other test is suspect. A limited number of comparisons with flight test data have been performed to date, including those shown in the results section of this paper. The second type of comparison is between the wind tunnel test and predictions. While it is normally the role of the experiment to provide validation data for the predictive tools, sometimes the predictions can help identify problems with the data. For example, comparisons of predicted section moments with flight-test data have helped identify suspect trailing edge pressures that had biased the mean section pitching moments. It is expected that both of these types of comparisons will continue for as long as the data are still being used.

Data Validation Examples

These data validation approaches have been applied to the acquired data to help identify suspect channels as well as validate good results. Two interesting examples are provided below.

Rotor Thrust

As stated earlier, the primary measurement of rotor thrust comes from the LRTA rotor balance. In addition, the thrust can be determined through two alternate methods. The first method begins with the integration of blade chordwise pressures at every radial station to determine section airloads. These airloads are then integrated along the radius to determine individual blade thrust and transformed to the fixed system (assuming identical blades) to determine overall rotor thrust. This integration procedure accounts for built-in blade twist and collective and cyclic pitch, but does not account for blade flexibility.

The second method combines the four hub arm vertical shear measurements, transforms the resultant load to the fixed system, and then adds in the control system loads to determine rotor thrust. Because the hub arm gages were affected by CF, the measurements were corrected prior to combining.

Figure 13 shows the comparison of thrust measurement methods for 80 different test conditions ranging from $\alpha_S=0$ to -7 deg, $\mu=0.15$ to 0.35 , and $C_T/\sigma=0.05$ to 0.13 . The data

are plotted as thrust ratio versus data point number, where thrust ratio is the integrated pressure or hub arm thrust divided by the rotor balance thrust. Although there is some variability, the thrust ratios for the integrated pressures are mostly low by 2-3% and for the hub arms are mostly high by 2%. An exact match was not expected, due to the limited number of radial stations used for integration, and the CF corrections necessary for the hub arm measurements. Nonetheless, the consistency of the measurements is reassuring. This is particularly true for the integrated thrust, since similar comparisons using flight test data (integrated thrust versus thrust derived from aircraft weight) showed differences up to 15% at some flight conditions (Ref. 1).

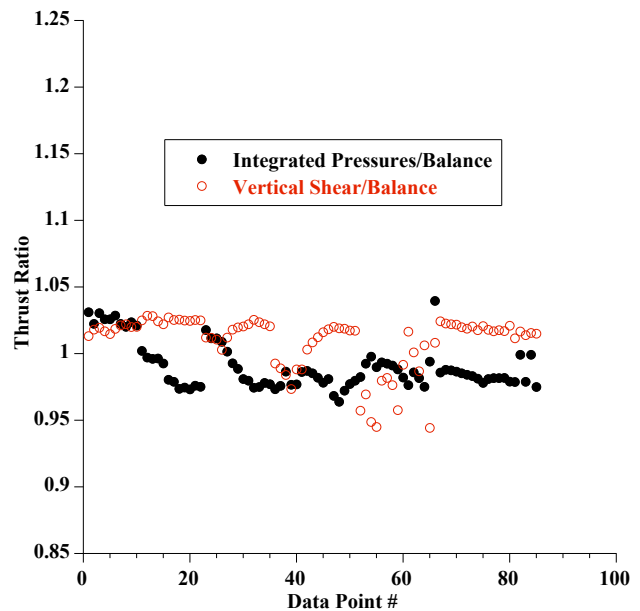


Figure 13. Rotor thrust ratios (normalized by balance thrust) for two alternate thrust calculations (integrated pressures, hub arm vertical shear) for a range of thrust and airspeed conditions.

Figure 14 shows the average time history of rotor thrust as calculated from the rotor balance and hub arm measurements for one flight condition ($\alpha_S=0$ deg, $M_{tip}=0.625$, $\mu=0.30$, $C_T/\sigma=0.08$). Although there are differences in the higher frequency content, the mean value and low frequency variations are quite similar between methods. The higher frequency differences were expected since dynamic calibration corrections have not yet been applied to the rotor balance measurements. Of note is that both methods show a 1/rev variation in thrust. This is the result of the blades being slightly out-of-track at this condition.

Airloads Rev-to-Rev Repeatability

Understanding the rev-to-rev repeatability is important for any test parameter, but particularly for the rotor airloads. During the Airloads flight test, the pressure and resultant

airload data were quite repeatable for most steady level-flight testing, except for the rotor stall conditions. This was also true for the wind tunnel data.

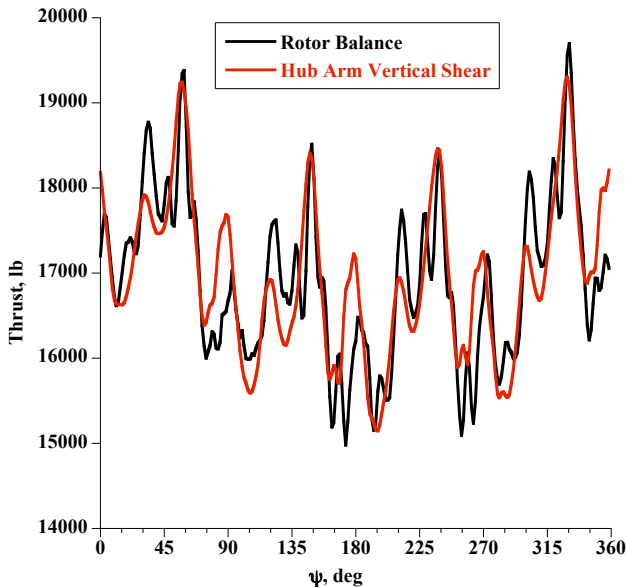


Figure 14. Comparison of rotor thrust time history from rotor balance and hub arm vertical shears ($C_T/\sigma=0.080$, $\alpha_s=0$ deg, $M_{tip}=0.625$, $\mu=0.30$).

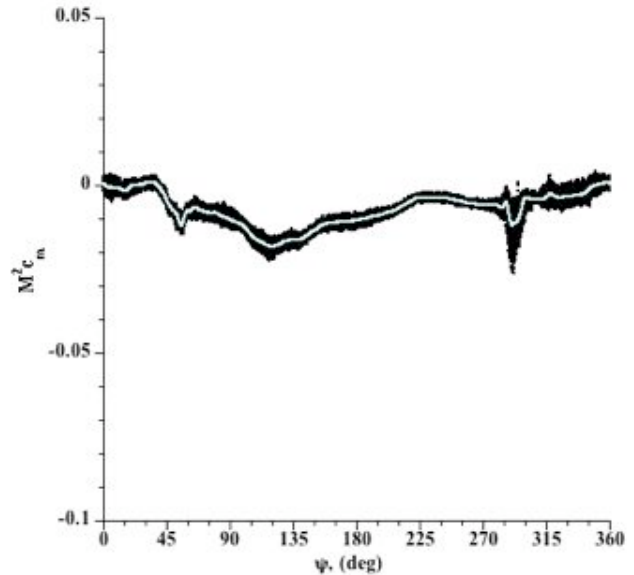
Figure 15 shows the time histories of integrated section pitching moment at $r/R=0.865$ for two thrust conditions. Included on each plot are data from all 128 revolutions of acquired data as well as the average. For the lower thrust case in Fig. 15a ($C_T/\sigma=0.10$), rev-to-rev variability is relatively small, except at the beginning of the small stall cycle at $\psi=290$ deg. For the deeply stalled case ($C_T/\sigma=0.125$) in Fig. 15b, the rev-to-rev variability is similar to the lower thrust case in the first 3 quadrants. In the fourth quadrant, the variability has increased significantly around the two stall cycles, indicative of the highly sensitive nature of the stall phenomena. Nonetheless, the average time history captures the means quite well and should allow for clear trends to be determined during critical parameter sweeps.

Data Validation Status

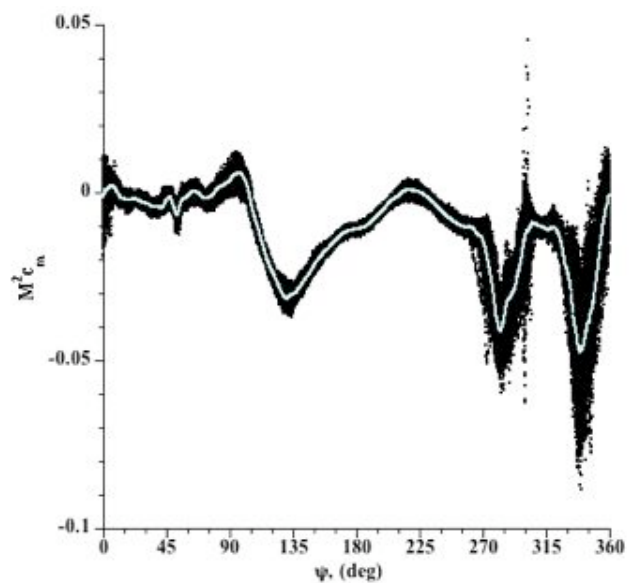
The ultimate goal is to verify the integrity of every measurement and derived parameter for every data point acquired during the test. Because of the large amount of data, this task has not yet been completed as of this writing. The current status of the data validation as it relates to some key parameters is provided in this section.

As mentioned earlier, a number of blade pressure transducers were replaced and wiring modified prior to the test so that 235 or the original 242 pressure transducers were

operational. After the first set of hover and forward flight runs, 20 of these transducers were shown to be suspect, leaving a total of 215 working transducers at the beginning of forward flight research testing. The distribution of these transducers was sufficient to provide valid integrated airloads at 8 of the 9 radial stations ($r/R=0.225, 0.4, 0.675, 0.775, 0.865, 0.92, 0.965, \text{ and } 0.99$). Unfortunately, the pressure transducers and/or their wiring continued to fail as forward-flight testing progressed. These failures were attributed mostly to internal problems with the 20-year-old wiring and were not repairable during testing. Ultimately, 55



a) $C_T/\sigma = 0.10$



b) $C_T/\sigma = 0.125$

Figure 15. Comparison of average $M^2 c_m$ to 128 individual revs for two different thrust conditions, including deep stall, ($\alpha_s=0$ deg, $M_{tip}=0.625$, $\mu=0.30$).

additional channels were considered highly questionable by the end of the test. If all 55 channels are eliminated from the integrations, only three radial stations remain with valid integrated airloads ($r/R=0.225, 0.865, \text{ and } 0.92$). Fortunately, many of the highest priority data points were acquired early in the test program when the majority of the transducers were working. In addition, it should be possible to correct the data (delete suspect revs, correct for drift, etc) for some of the suspect channels; this will, however, require significant effort for each channel and test condition corrected.

All of the blade bending measurements (normal bending, edgewise bending, torsion), control loads (pitch link loads) and shaft/hub loads (shaft moments, hub arm vertical shears) were operational at the start of the test. Similar to the blade pressure transducers, some of these failed as the test progressed. However, since these gages were more readily accessible, they were repaired between runs whenever possible. By the end of the test, a number of gages still had intermittent problems. As suggested for the blade pressure data, it should be possible to correct the data from most of these channels by deleting suspect revs from the averages.

All of the blade root motion transducers (12 for BMH and 12 for laser) were working at the start of the test. Like the other rotating measurements, there were some failures during testing with repairs attempted whenever possible. Comparisons of the resultant blade root motions between the BMH and laser sensors (as well as with the Blade Displacement system) show some differences between measurement systems, especially with the mean values. An evaluation to determine the cause of these differences (calibrations, drift, etc.) is currently underway.

TEST OBJECTIVES, APPROACH AND TEST CONDITIONS

The primary objective of this test program was to acquire a comprehensive set of validation-quality measurements on a full-scale pressure-instrumented rotor system at conditions that challenge the most sophisticated modeling and simulation tools. This included going beyond the conventional flight envelope, including to slowed rotor (high advance ratio) conditions. A secondary objective was to meet one of the original goals of the UH-60A Airloads program, that is to provide data to evaluate the similarities and differences between small-scale wind tunnel, full-scale wind tunnel, and full-scale flight tests.

To accomplish these objectives, the testing was separated into six phases: 1) 1-g level flight sweeps, 2) parametric sweeps, 3) Airloads flight test simulation, (4) small-scale wind tunnel test simulation, (5) slowed rotor testing, and (6) PIV testing. Except for the PIV phase, which reproduced

specific wake dominated points from earlier testing, each phase had a different objective, covered a different parameter space, and consequently required a different testing approach. A discussion of each test phase, including a summary of acquired test conditions, is provided in the sections below.

1-g Level Flight Sweeps

The objective of the 1-g level flight sweeps was to provide data that showed the effects of advance ratio for representative flight conditions, including various levels of aircraft weight. A level flight sweep is a speed sweep where the conditions (shaft angle, trim targets) are left to vary from one speed to another in order to achieve the vertical force and propulsive force targets expected to occur in flight. Representative trim conditions for the wind tunnel test were determined through a series of pre-test calculations where aircraft weight, M_{tip} , fuselage drag, and aircraft c.g. position were assumed constant. These calculations provided the target lift, propulsive force, and hub moments to be used during testing.

For each wind tunnel test condition, the rotor RPM and tunnel speed were set to match the target M_{tip} and μ , and the shaft angle set to match the predicted value. The trim controller then targeted the appropriate lift and hub moments and estimated the shaft angle change necessary to match propulsive force. The lift and propulsive force used as targets included corrections for wind tunnel wall effects. The shaft angle was then manually adjusted until all trim targets were met.

The 1-g level flight sweeps were performed at three lift levels, $C_L/\sigma=0.08, 0.09, \text{ and } 0.10$, up to an advance ratio of $\mu=0.4$. A summary of the test conditions is provided in Table 4.

Table 4. 1-g Level Flight Test Conditions

C_L/σ	μ	M_{tip}
0.08	0.15, 0.20, 0.24, 0.30, 0.35, 0.37, 0.385, 0.40	0.650
0.09	0.15, 0.20, 0.24, 0.30, 0.35, 0.37, 0.385, 0.40	0.650
0.10	0.15, 0.20, 0.24, 0.30, 0.35, 0.37, 0.385	0.650

Parametric Sweeps

The objective of the parametric sweeps was to provide data over a wide range of conditions to show the effects of thrust (C_T/σ), advance ratio (μ), shaft angle (α_S), and tip Mach number (M_{tip}) on rotor loads. The ability to precisely control variations of trim parameters and to test outside the normal flight envelope was expected to be quite valuable. In

particular, the resultant data would allow evaluation of rotor airloads during low speed descent (low speed, positive shaft angle), rotor stall (moderate speed, high thrust), and higher advancing Mach number conditions (high speed, high M_{tip}).

For each wind tunnel test condition, the rotor RPM, tunnel speed, and shaft angle were set to match the target M_{tip} , μ , and α_s . The trim controller then targeted the appropriate rotor thrust (C_T/σ), and zero fixed-system hub moments. A thrust sweep was performed at each set of conditions until limits were reached. If these limits were associated with rotor stall, collective pitch was manually varied to better define the phenomena. During the collective sweeps, the trim controller only controlled hub moments.

The parametric sweeps were conducted at three different tip Mach numbers, with the majority of data acquired at the baseline $M_{tip}=0.650$. A limited number of sweeps at $M_{tip}=0.625$ were conducted to attain higher non-dimensional thrusts and advance ratios without reaching load limits. A limited number of sweeps at $M_{tip}=0.675$ were also conducted, with the objective of exploring higher advancing blade Mach numbers. A summary of all parametric test conditions is provided in Table 5.

Table 5. Parametric Sweep Test Conditions

M_{tip}	α_s	μ	C_T/σ
0.650	-8	0.30	.02 to .12
		0.35	.02 to .11
		0.37	.02 to .11
	-4	0.15	.08
		0.24	.02 to .126
		0.30	.02 to .118
		0.35	.02 to .11
		0.15	.04 to .13
	0	0.20	.04 to .13
		0.24	.02 to .127
		0.30	.02 to .124
		0.35	.02 to .11
		0.15	.06 to .13
	4	0.20	.02 to .12
		0.24	.02 to .12
		0.30	.06 to .08
		0.15	.06 to .12
		0.20	.06 to .12
8	0.24	.06 to .12	
	0.30	.08	
	0.24	.02 to .131	
	0.30	.02 to .125	
0.625	0	0.24	.02 to .131
0.675	-8	0.35	.02 to .10
		0.37	.02 to .10
		0.385	.02 to .09

Airloads Flight Test Simulation

The objective of this phase of testing was to examine the similarities and differences between flight test and full-scale wind tunnel data. This was accomplished by attempting to reproduce several Airloads Program flight test points (Ref. 1). The measured flight test data included aircraft weight, airspeed, hub moments (derived from a shaft bending gage), rotor RPM, and rotor shaft angle. The rotor thrust was determined using aircraft weight and an estimate of non-rotor lift (fuselage, tail rotor, etc.). These flight test parameters were non-dimensionalized and then used to set the wind tunnel baseline conditions. To compensate for uncertainties in the flight test conditions (and limitations in reproducing them in the tunnel), additional wind tunnel data were acquired for derivative points around this baseline. These derivatives included changes in thrust, hub moment, and shaft angle.

For each simulated flight condition, the rotor RPM and tunnel speed were set to match the target M_{tip} and μ , and the shaft angle was set so the wind tunnel wall corrected angle, α_c , matched the flight test. The trim controller then targeted the appropriate rotor thrust (C_T/σ), and fixed system hub moments (derived from the same shaft bending gage used in flight). If necessary, the shaft angle was further adjusted to match α_c exactly.

A total of three Airloads flight test points were simulated; C8525, C8424, and C9020. A summary of these test conditions is provided in Table 6.

Table 6. Flight/DNW Test Simulation Conditions

Test	Test Pt #	M_{tip}	μ	C_T/σ
Flight	C8424	0.638	0.30	0.087
	C8525	0.643	0.23	0.077
	C9020	0.669	0.245	0.118
DNW	11.24	0.629	0.30	0.10
	13.12	0.638	0.30	0.07
	13.20	0.637	0.15	0.07

Small-Scale Wind Tunnel Test Simulation

Similar to the flight test simulation, the objective of this phase was to examine the similarities and differences between small-scale and full-scale wind tunnel data. This was accomplished by reproducing several small-scale tunnel test points acquired in the Duits Nederlands Windtunnel (DNW, Ref. 7). The measured DNW data included C_T/σ , M_{tip} , μ , and α_s , with the primary trim procedure to minimize 1/rev flapping. To match these conditions in the NFAC, it was necessary to match the corrected shaft angle, α_c , where corrections were necessary for both wind tunnels. Similar to the flight test, both baseline and derivative data points were

acquired. For each simulated DNW condition, the rotor RPM and tunnel speed were set to match the target M_{tip} and μ , and the shaft angle set so the wind tunnel wall corrected angle, α_c , matched the DNW test. The trim controller then targeted the appropriate rotor thrust (C_T/σ), and minimized 1/rev flapping (from the pressure blade flap RVDT). If necessary, the shaft angle was further adjusted to match α_c exactly.

A total of three DNW test points were simulated; 11.24, 13.12, and 13.20. A summary of these test conditions is provided in Table 6.

Slowed Rotor Testing

The objective of the slowed rotor testing was to evaluate non-conventional operating envelopes made possible by large reductions in rotor RPM. This included testing to very high advance ratios, up to $\mu=1.0$. Since this testing required the UH-60A to fly well outside its normal operating envelope, the testing procedures were modified to minimize the possibility of stability or structural issues. In particular, the shaft angle and tip Mach number were set prior to increasing tunnel speed and no significant variations were permitted outside of hover.

For each wind tunnel test condition, the rotor RPM, tunnel speed, and shaft angle were set to match the target M_{tip} , μ , and α_s . Rotor 1/rev flapping was minimized at all times. A collective pitch sweep was performed at each advance ratio until limits were reached. The trim controller was not used during this phase of testing.

The collective sweeps were conducted at $M_{tip}=0.650$, 0.420, and 0.260 (approximately 100%, 65%, and 40% of nominal RPM). Data were acquired for three shaft angles at advance ratios from 0.3 to 1.0. The maximum advance ratio at each RPM was limited by the predefined tunnel limit of 180 kt. A summary of all test conditions is provided in Table 7.

PIV Testing

The objective of the PIV testing was to acquire detailed flow-field velocity measurements at well-documented test conditions to better understand the flow physics as well as provide unique data for validation. This phase of testing consisted of acquiring PIV data for a limited number of forward flight conditions where data had been previously acquired. This testing was conducted as a separate phase for a number of reasons, including the need for long data preparation/acquisition times, low tunnel lighting, and the concern that the tunnel seeding material (mineral oil) might contaminate the blade pressure taps. This latter concern prompted the sealing of all pressure taps with tape prior to

PIV testing. As it turned out, this concern was unfounded and the tape was removed after the first few PIV runs.

The trim procedures used for each test condition were identical to those used when the data were originally acquired. The primary difference was the length of time the trim controller operated as a result of the longer PIV data acquisition time. NFAC DAS data were also acquired over this entire period (3 consecutive data points of 256 revolutions) to provide valid average flight conditions during the PIV measurements.

PIV data were acquired at 11 different flight conditions for a number of different azimuth delays (rotor blade azimuths relative to the PIV measurement plane). This resulted in a total of 57 PIV data sets acquired. A summary of all PIV test conditions is provided in Table 8.

Table 7. Slowed Rotor Test Conditions

M_{tip}	α_s	μ	θ_0	
0.650	0	0.30	0, 2, 3, 4, 6, 8, 10	
		0.40	0.5, 2, 3, 4, 6, 8	
	2	0.30	0, 2, 3, 4, 6, 8, 10	
		0.40	0, 2, 3, 4, 6, 8	
	4	0.30	0, 2, 3, 4, 6	
		0.40	0, 2, 3, 4, 6	
	0.420	0	0.30	0, 2, 3, 4, 6, 8
			0.40	0, 2, 3, 4, 6, 8
0.50			0, 2, 3, 4, 6, 8	
0.60			0, 2, 3, 4, 6, 8	
2		0.30	0, 2, 3, 4, 6, 8	
		0.40	0, 2, 3, 4, 6, 8	
		0.50	0, 2, 3, 4, 6, 8	
		0.60	0, 2, 3, 4, 6, 8	
0.260	0	0.30	0, 2, 3, 4, 6, 8	
		0.40	0, 2, 3, 4, 6, 8	
		0.50	0, 2, 3, 4, 6, 8	
		0.60	0, 2, 3, 4, 6, 8	
		0.70	0, 2, 3, 4, 6, 8	
		0.80	0, 2, 3, 4, 6, 8	
		0.90	0, 2, 3, 4	
		1.00	0, 1, 2	
	2	0.30	2	
		0.40	2	
		0.50	2	
		0.60	2	
4	0	0.70	2	
		0.80	2	
		0.90	2	
		1.00	1	
	2	0.30	0, 2, 3, 4, 6, 8	
		0.40	0, 2, 3, 4, 6, 8	
		0.50	0, 2, 3, 4, 6, 8	
		0.60	0, 2, 3, 4, 6, 8	
4	0.70	0, 2, 3, 4, 6, 8		
	0.80	0, 2, 3, 4, 6, 8		
	0.90	0, 2, 3, 6		
	1.00	0, 2		

Table 8. PIV Test Conditions

M_{tip}	α_s	μ	C_T/σ	Azimuth delay
0.65	0	0.15	0.08	5, 15, 30, 45, 60, 75, 95, 135, 185, 225, 275, 315
0.65	4	0.15	0.08	5, 15, 30, 45, 60, 75, 95, 135, 185, 225, 275, 315
0.638	-	0.30	0.087	5, 15, 30, 45, 60, 75, 95
0.65	0	0.24	0.07, 0.09	5
0.65	0	0.24	0.11	5, 15, 30, 45, 60, 75, 95, 185, 275
0.65	0	0.15	0.07, 0.09, 0.11, 0.12	15
0.65	-6.9	0.35	0.08	5, 10, 15, 20, 30, 45, 60, 75, 95, 185, 275

SAMPLE RESULTS

In this section, sample results are provided for each of the six test phases described above.

1-g Level Flight Sweeps

Rotor performance results for the three 1-g level flight sweeps (up to $\mu=0.40$) are presented in Figs. 16 and 17. As expected (Ref. 3), the rotor power increases rapidly at higher advance ratios (Fig. 16) due to drag increases from supercritical flow on the advancing side. Figure 17 shows the rotor lift to drag ratio (L/D_e) is optimal at $\mu=0.30$ and $C_L/\sigma=0.08$. At other speeds and at higher lift, the L/D_e is reduced.

Figure 18 shows the normal force distribution along the blade and around the azimuth for the highest-speed flight condition ($\mu=0.40$) at $C_L/\sigma=0.09$. This radial contour plot shows many of the features expected in high-speed forward flight, including negative lift near the tip in the second quadrant to accommodate roll moment balance as well as negative lift on the inboard sections of the retreating blade due to reverse flow. The lift distribution varies around the azimuth with the highest lift near the forward and aft sections of the rotor.

A more detailed look at the section airloads for a single radial station ($r/R=0.92$) is provided in Figs. 19 and 20. These figures show the variations in normal force and moment (M^2c_n and M^2c_m) for increasing advance ratio. At low speeds, the effect of vortex induced loading can be seen on both the advancing and retreating side (approximately $\psi=70$ and 280 deg) up to $\mu=0.30$. As advance ratio is increased, the section normal force is redistributed (Fig. 19),

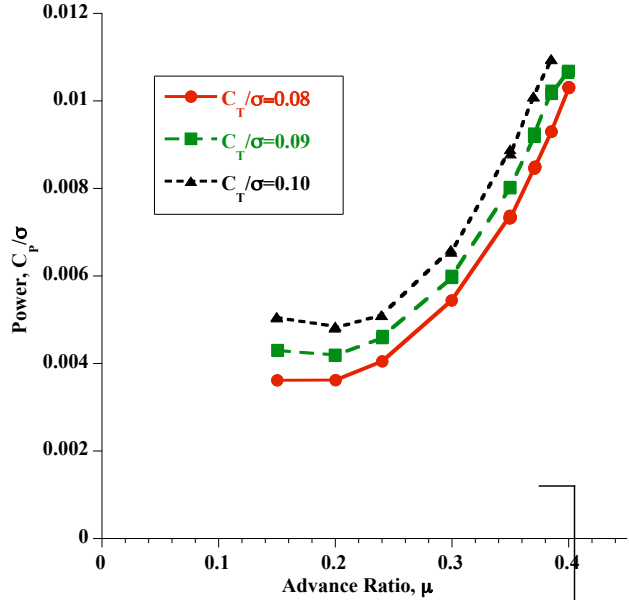


Figure 16. Rotor Power for three 1-g forward flight sweeps.

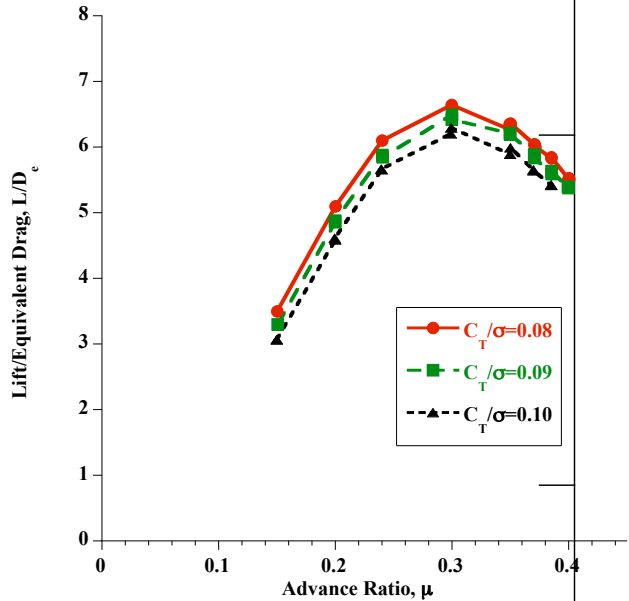


Figure 17. Rotor lift to equivalent drag ratio for three 1-g forward flight sweeps.

with increases in the first quadrant to go along with decreases in the second. These data also show the peak of the negative lift occurring at earlier azimuth positions as advance ratio is increased.

Figure 20 shows the large negative pitching moments that develop on the advancing side as advance ratio is increased. Unlike the lift, however, the peak of the negative moment occurs at later azimuth positions as advance ratio is increased. Also shown in this figure is the development of a

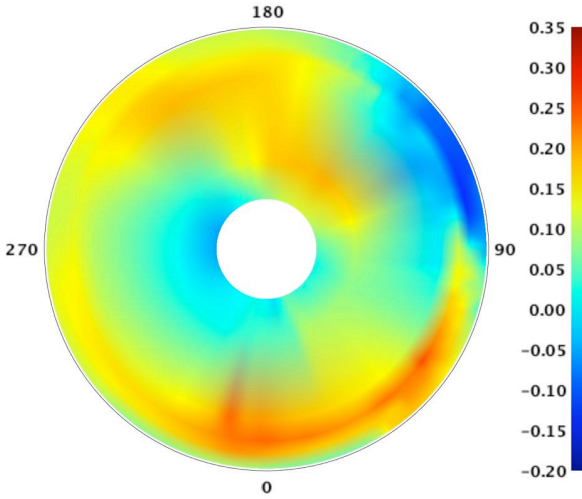


Figure 18. Contour plot of M^2c_n at high speed ($C_T/\sigma=0.09$, $M_{tip}=0.650$, $\mu=0.40$).

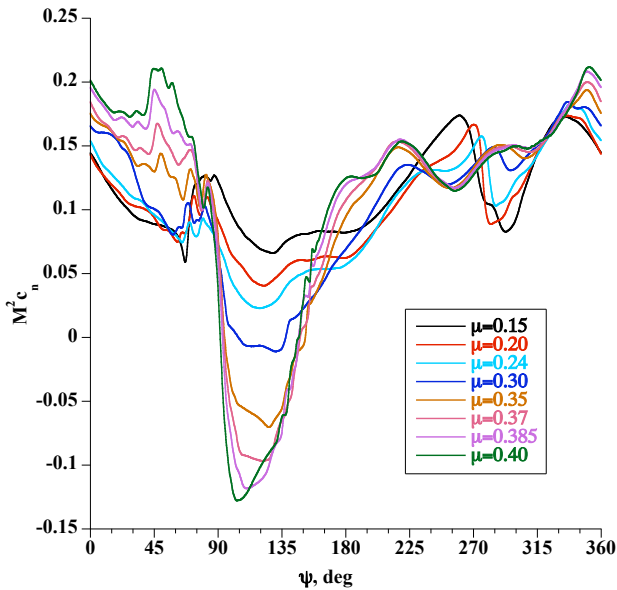


Figure 19. M^2c_n time history as a function of advance ratio, $r/R=0.92$, $C_T/\sigma=0.09$, $M_{tip}=0.650$.

sharp moment pulse at approximately $\psi=90$ deg for advance ratios above $\mu=0.30$. This azimuth location and advance ratio is consistent with the development of supercritical flow over the upper surface of the blade.

These data suggest that the 1-g speed sweeps can provide a worthy complement to similar level-flight sweeps performed during the Airloads flight test. The addition of new and/or improved measurements (including rotor performance), as well as acquisition of data at higher advance ratios, provides even greater value.

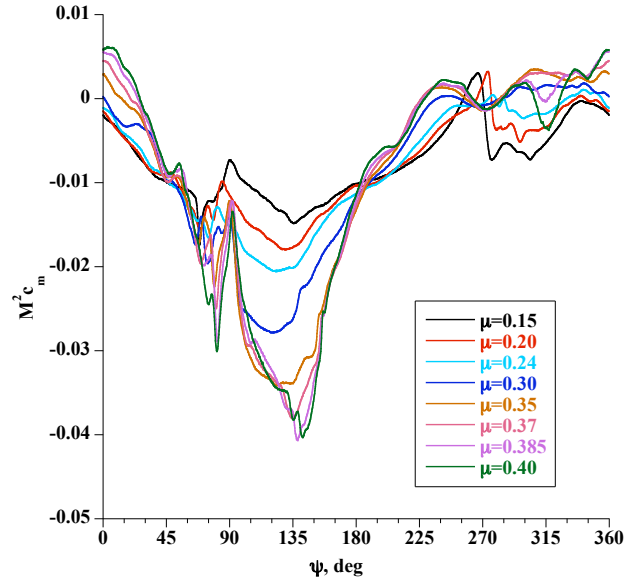


Figure 20. M^2c_m time history as a function of advance ratio, $r/R=0.92$, $C_T/\sigma=0.09$, $M_{tip}=0.650$.

Parametric Sweeps

As noted earlier, parametric sweeps were performed over a wide range of rotor and wind tunnel conditions. During six of these sweeps, small collective pitch variations up to the maximum rotor or wind tunnel limits were performed to help better understand the development of dynamic stall. Figure 21 shows the rotor thrust as a function of collective pitch for four of these sweeps. The presence of stall for each sweep is confirmed by the roll-off of thrust for increasing values of pitch. The data at $\mu=0.30$ should be particularly valuable since the flight test did not include stall conditions at this high speed.

The normal force and moment distributions for one dynamic stall test condition are shown in Fig. 22. These contour plots are for the highest collective ($\theta_0=12.3$ deg, $C_T/\sigma=0.125$) achieved during one of the stall sweeps ($\alpha_S=0$ deg, $M_{tip}=0.625$, $\mu=0.30$). The normal force distribution in Fig. 22a shows a significantly different loading distribution than that for the high-speed condition (Fig. 18). In particular, there are now four areas of reduced lift near the blade tip (instead of one) as well as four distinct high lift areas. The moment distribution in Fig. 22b shows three areas near the blade tip with large negative pitching moments. The two on the retreating side are consistent with dynamic stall cycles as seen previously during flight test (Ref. 4).

A more detailed look at the section airloads for a single radial station ($r/R=0.92$) is provided in Figs. 23 and 24. These figures show the variations in normal force and moment (M^2c_n and M^2c_m) for increasing collective. Figure 23 shows a number of interesting features, including

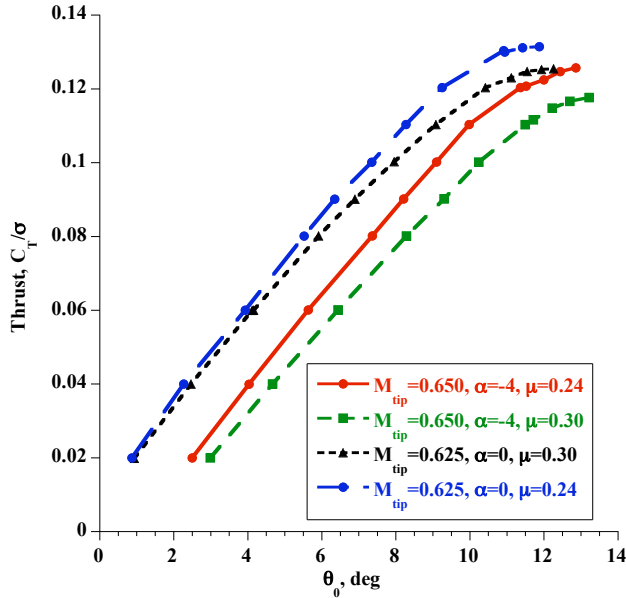


Figure 21. Rotor thrust vs. collective for four dynamic stall parametric sweeps.

increasingly negative lift on the advancing side (for roll moment balance) as well as indications of lift stall at azimuth angles of approximately $\psi=290$ and 340 deg. The first suggestion of a lift stall cycle shows up as early as $\theta_0=4.1$ deg ($C_T/\sigma=0.06$).

Figure 24 shows the development of the two moment stall cycles on the retreating side. The first negative peak appears at $\theta_0=9.1$ deg ($C_T/\sigma=0.11$) at $\psi=290$ deg. As collective is increased, the magnitude of the peak stabilizes above $\theta_0=10.4$ deg ($C_T/\sigma=0.12$) although the location of the peak continues to move to earlier azimuth positions. The second stall cycle first appears at $\theta_0=10.4$ deg. As collective is increased, the magnitude of the peak continues to grow, although the location of the peak ($\psi=330$ deg) does not change.

The ability to perform controlled variations during the parametric sweeps has provided a unique set of data for validation, including data at many conditions outside the normal flight envelope. The data acquired during the dynamic stall sweeps should be especially valuable, helping to define the sensitivity of collective pitch (and thrust) to the onset and development of stall.

Airloads Flight Test Simulation

Figures 25 and 26 provide the initial comparisons of integrated airloads between a flight test data point (c8424) and simulated flight conditions from the wind tunnel. Each plot shows the flight test data, the baseline wind tunnel data, and two derivative data points ($C_T/\sigma=\pm 0.005$). Only the

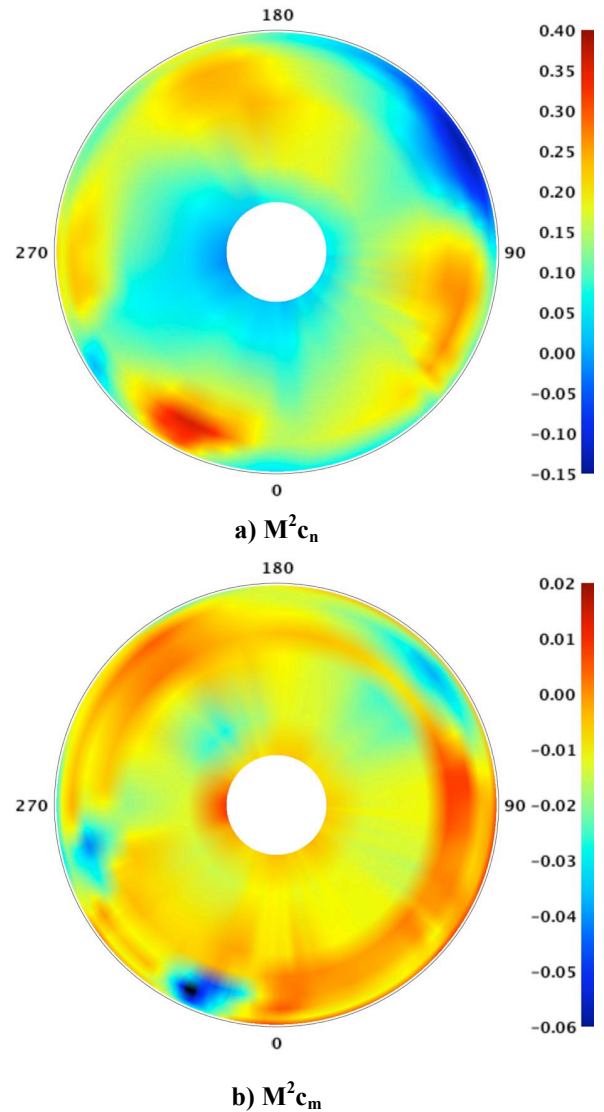


Figure 22. Contour plots of M^2c_n and M^2c_m during dynamic stall ($C_T/\sigma=0.125$, $\alpha_s=0$ deg, $M_{tip}=0.625$, $\mu=0.30$).

thrust derivatives are displayed because none of the other derivative points showed a significant effect on the airloads.

Figure 25 shows the normal force, moment, and chord force at $r/R=0.4$. At this inboard station, both the normal and chord forces match well with the flight test data, while the moment has a large offset. As noted in previous papers, the mean section moments are particularly sensitive to the pressure readings near the blade trailing edge and a number of them were suspect during both the flight and wind tunnel test. Further analysis will be required to determine which mean section moment value, if any, is correct.

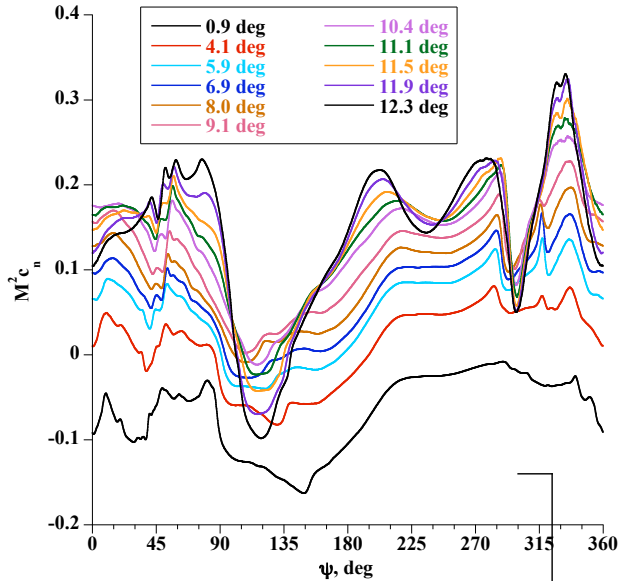


Figure 23. $M^2 c_n$ time history as a function of collective, $r/R=0.92$, $\alpha_S=0$ deg, $M_{tip}=0.625$, $\mu=0.30$.

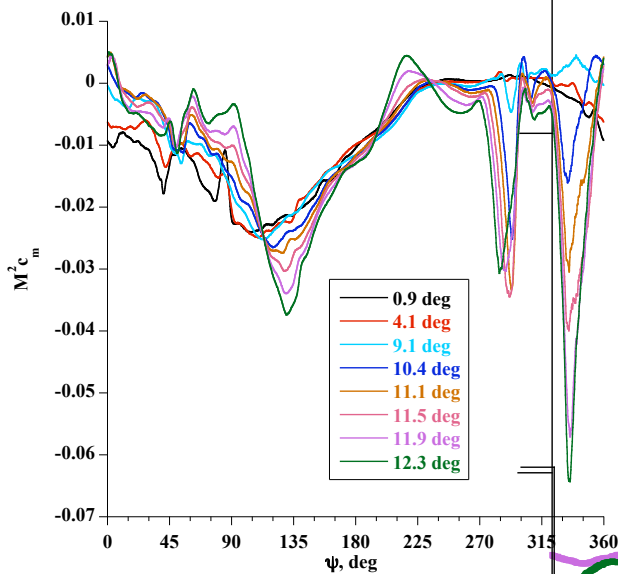


Figure 24. $M^2 c_m$ time history as a function of collective, $r/R=0.92$, $\alpha_S=0$ deg, $M_{tip}=0.625$, $\mu=0.30$.

Figure 26 shows the normal force, moment, and chord force at $r/R=0.865$. The data at this radial station show significantly larger differences. This is particularly true for the normal force, where the flight test data show a narrower and deeper negative peak on the advancing side and a higher positive peak on the retreating side. The section moments once again are slightly offset from each other, and also show some differences in waveform following the negative peak on the advancing side. Finally, the chord forces match very well on the retreating side but have a small offset on the advancing side.

The differences between the data sets are not yet fully understood. Further analysis is necessary to determine whether the differences are due to local aerodynamic effects of the wind tunnel walls or simply a difference in the quality of specific pressure transducer measurements. The initial results do suggest, however, that the differences are probably not caused by differences in the definition of the flight test trim condition.

Small-Scale Wind Tunnel Test Simulation

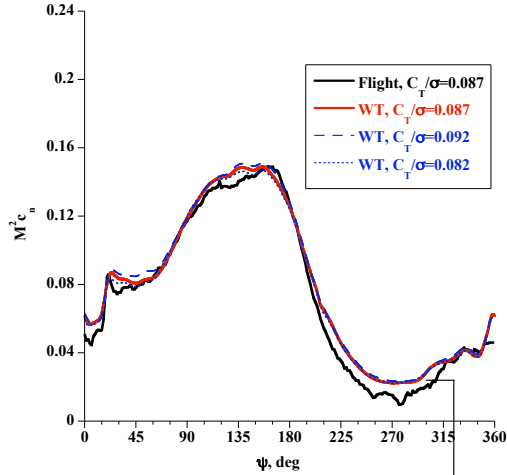
Figure 27 provides an initial comparison of integrated normal force between a DNW test data point (13.20) and simulated conditions from the wind tunnel. Each plot shows the DNW test data, the baseline wind tunnel data, and two derivative data points ($\Delta C_T/\sigma = \pm 0.005$). Only the thrust derivatives are displayed because none of the other derivative points showed a significant effect on the airloads.

Figure 27a shows the normal force at $r/R=0.4$. Although similar in character, there are some noticeable differences. In particular, the DNW peak lift on the advancing side occurs at an earlier azimuth, the lift on the retreating side has a deeper negative peak, and lift is significantly lower behind the rotor at $\psi=0$ deg. Figure 27b shows the normal force at $r/R=0.865$. The data at this radial station show significantly larger differences. Similar to the flight test comparisons (Fig. 26a), the DNW data show a narrower and deeper negative peak on the advancing side and a higher positive peak on the retreating side. Once again, the DNW lift is significantly lower behind the rotor.

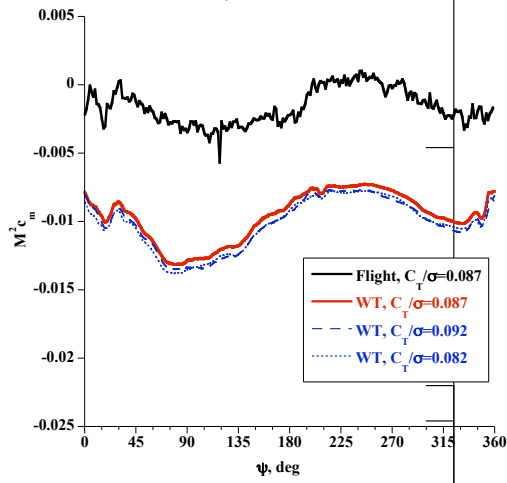
Previous comparisons between DNW and flight test data (Refs. 1, 27) suggest that the lower DNW lift behind the rotor is likely caused by the relatively larger instrumentation hat used during DNW testing. Many of the other differences are likely the result of differences in the blade torsional properties between the small- and full-scale blades (Ref. 28). Further data analysis is necessary to confirm these observations and/or to identify other factors that may also contribute to the observed differences.

Slowed Rotor Testing

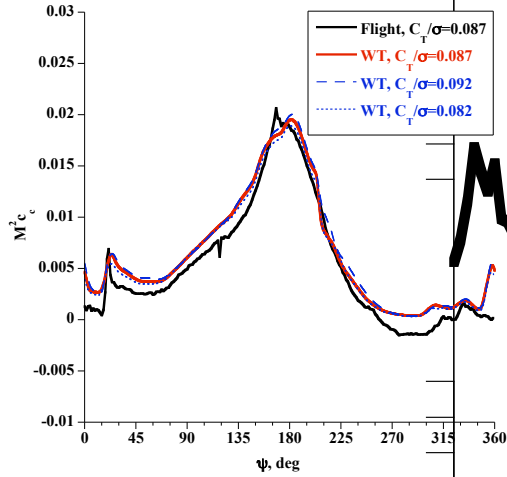
The slowed rotor testing produced very unique data that can be used to better understand the aerodynamic and dynamic environment of rotors at high advance ratio. Figures 28 and 29 provide a sample from these data, showing the thrust vs. collective angle and power vs. thrust for fixed advance ratios at $M_{tip}=0.260$ and $\alpha_S=0$ deg. The sensitivity of thrust to collective disappears beyond $\mu=0.8$ and the sensitivity of power to thrust reverses. These and other data (including performance, blade pressures, section airloads, structural loads and hub loads) are reviewed in detail in Ref. 8.



a) $M^2 c_n$

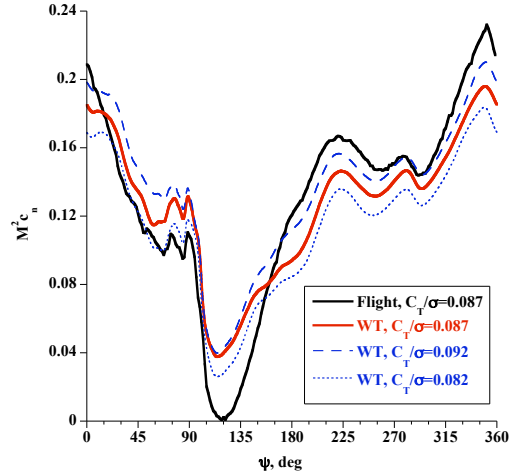


b) $M^2 c_m$

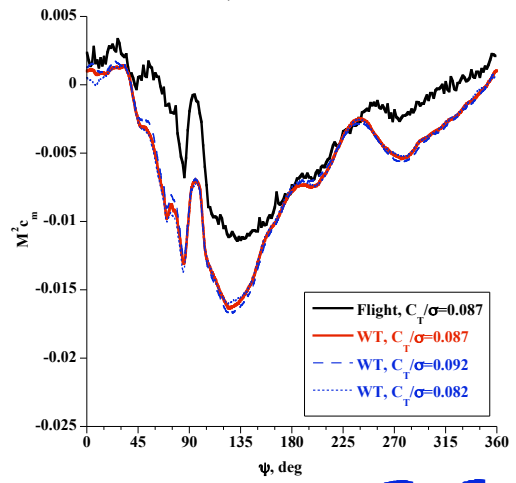


c) $M^2 c_c$

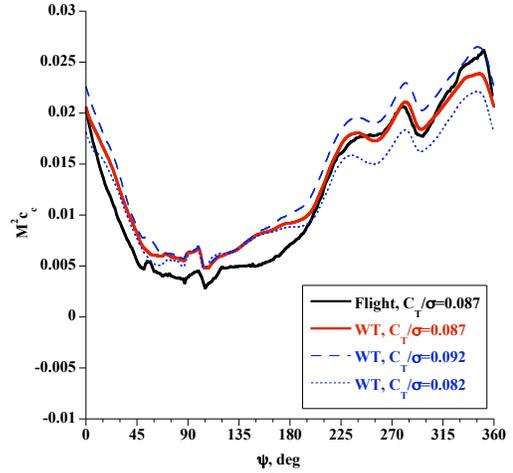
Figure 25. Comparison of integrated airloads ($M^2 c_n$, $M^2 c_m$, $M^2 c_c$) with Airloads Flight Test data (flight counter c8424) including derivatives of thrust, $r/R=0.40$ $C_T/\sigma=0.087$, $M_{tip}=0.638$, $\mu=0.30$.



a) $M^2 c_n$

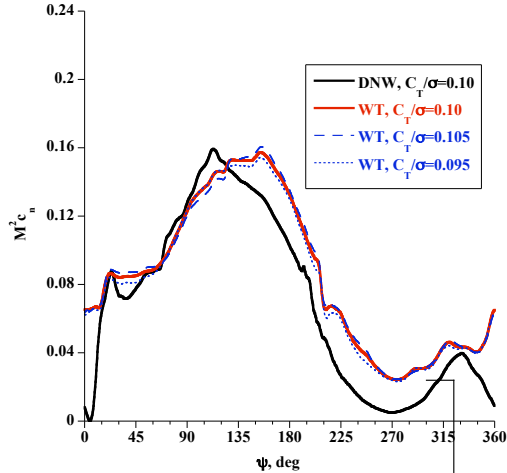


b) $M^2 c_m$

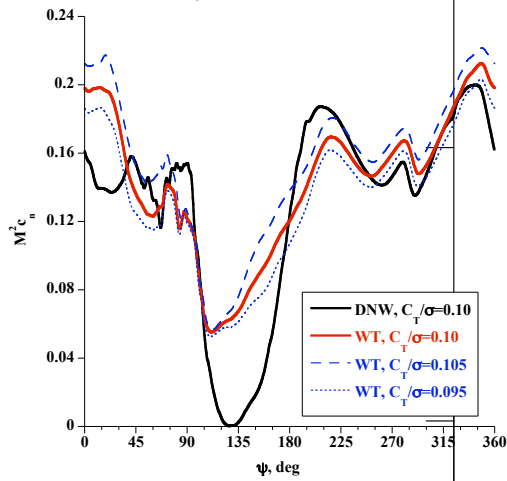


c) $M^2 c_c$

Figure 26. Comparison of integrated airloads ($M^2 c_n$, $M^2 c_m$, $M^2 c_c$) with Airloads Flight Test data (flight counter c8424) including derivatives of thrust, $r/R=0.865$, $C_T/\sigma=0.087$, $M_{tip}=0.638$, $\mu=0.30$.



a) $r/R = 0.40$



b) $r/R = 0.865$

Figure 27. Comparison of integrated normal force ($M^2 c_n$) with DNW wind tunnel data (DNW point 13.20) including derivatives of thrust, $r/R=0.865$, $C_T/\sigma=0.10$, $M_{tip}=0.629$, $\mu=0.30$.

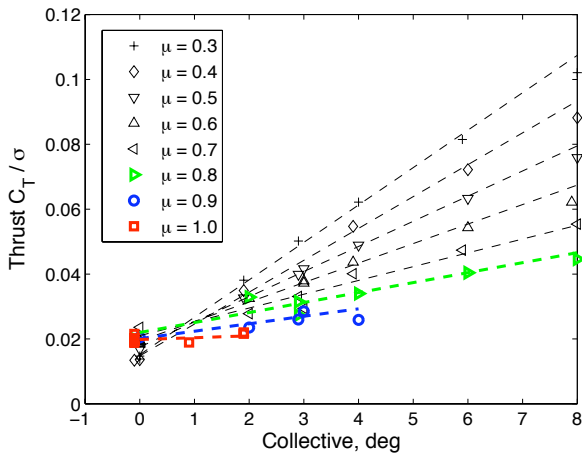


Figure 28. Thrust vs. collective for fixed advance ratios at $M_{tip}=0.260$ and $\alpha_s=0$ deg.

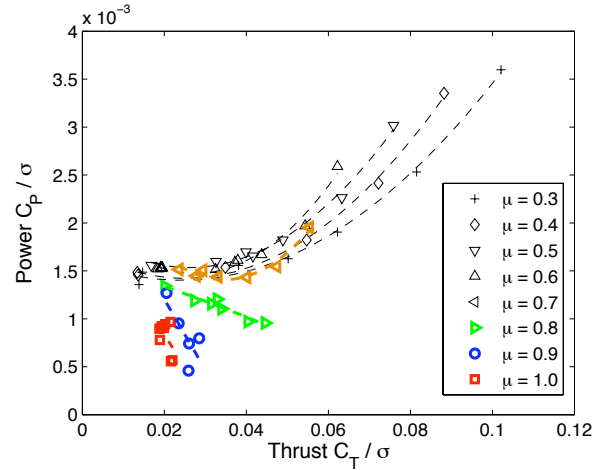


Figure 29. Power vs. thrust for fixed advance ratios at $M_{tip}=0.260$ and $\alpha_s=0$ deg.

PIV Testing

As discussed earlier, reduction of the PIV data is currently underway. In order to get a preliminary assessment of the data, simple ensemble averages for the velocity field have been computed for each test condition. Figure 30 shows an average velocity field for one of these conditions ($\alpha_s=0$ deg, $M_{tip}=0.650$, $C_T/\sigma=0.080$, $\mu=0.15$). The delayed azimuth, that is, the blade azimuth relative to the laser light sheet, is 30 degrees. The coordinates $(r/R, z/R)=(1,0)$ define the intersection of the blade tip trailing edge with the laser sheet at delayed azimuth equals 0 degrees. For clarity, every other in-plane vector is shown. Primary features of the flow field are clearly visible, including the blade trailed wake (identified by the velocity defect in the streamwise velocity contour) and vortices, indicated by several concentrations of swirling in-plane vectors. The location of the discontinuities in the blade trailed wake ($r/R=0.74$ and 0.86) are consistent with the location and upward deflection of the blade trailing edge trim tab. Figure 31a and 31b show expanded views of the vorticity field near the outer 20% of the blade for delayed azimuths of 5 deg and 30 deg, respectively. As expected, a strong tip vortex can be observed near $r/R=1$, in addition to vortices from previous blade passages. The vortex produced from the outboard end of the trim tab can also be observed, though much weaker in strength and of opposite sign compared to the tip vortex. The effects of wake age on vorticity can be seen by comparing Fig. 31b with 31a. For example, the tip vortices are clearly weaker and have migrated inboard at the later wake age.

As mentioned earlier, these results come from preliminary data processing. Final data reduction will require a number of additional steps, including image processing that corrects for laser sheet movement, separate calibrations for the inner and outer half of the ROI, smaller cross-correlation windows

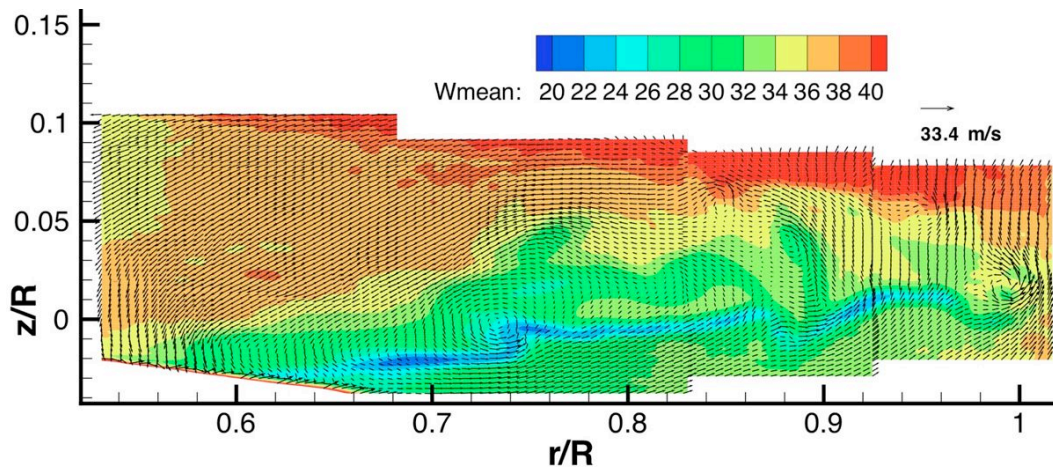
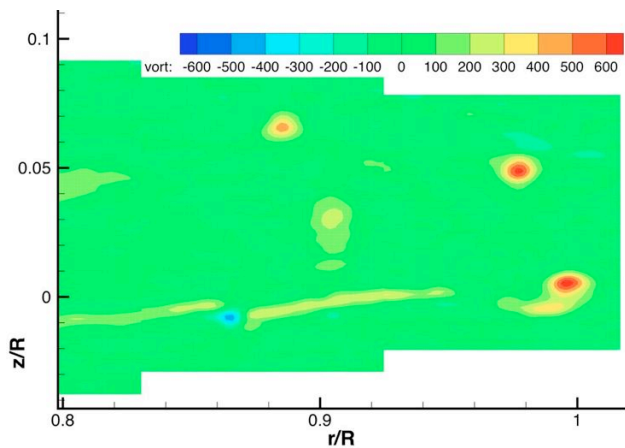
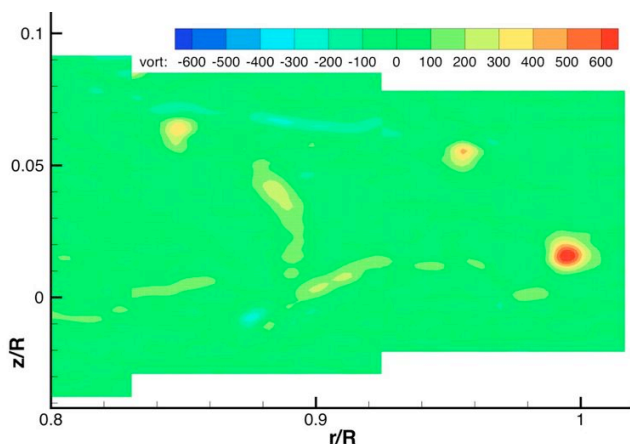


Figure 30. Ensemble average of velocity field, $\alpha_s=0$ deg, $M_{tip}=0.650$, $C_T/\sigma=0.080$, $\mu=0.15$, test section velocity (W_{mean}) = 33 m/s. Azimuth delay = 30 deg, view looking upstream, every other vector shown.



a) Azimuth delay = 5 deg



b) Azimuth delay = 30 deg

Figure 31. Ensemble average of vorticity field, $\alpha_s=0$ deg, $M_{tip}=0.650$, $C_T/\sigma=0.080$, $\mu=0.15$, test section velocity = 33 m/s. View looking upstream.

with greater overlap, and conditional averaging of the vector fields. Still, these results provide a clear indication of the richness of the PIV data acquired.

CONCLUDING REMARKS

A full-scale wind tunnel test of the UH-60A airloads rotor was recently completed in the NFAC 40- by 80-Foot Wind Tunnel. The present paper has provided an overview of the test, including detailed descriptions of the hardware, instrumentation, and data acquisition and reduction systems. In addition, the data validation process, the test objectives and approach, and some sample results were presented. Based on the data evaluated to date, the following observations are made:

- 1) The test has produced unique data not available from the Airloads flight test, including data from new measurements as well as data acquired at conditions outside the conventional flight envelope. The new measurements included rotor balance forces and moments, oscillatory hub loads, blade displacements and deformations, and rotor wake measurements. The new flight conditions included 1-g flight simulations up to $\mu=0.40$, parametric sweeps at non-standard conditions, including multiple sweeps into stall, and slowed rotor simulations up to $\mu=1.0$. These new data should provide an excellent resource for validating new and emerging predictive tools.
- 2) Although further data evaluations must be performed to clearly identify all valid measurements as a function of data point, the quality of the data is generally very good. The addition of the new rotor balance, hub, and shaft measurements will help minimize the uncertainties

associated with rotor trim from the flight test. In addition, the three new independent measurement systems (Blade Displacement, PIV, RBOS) will provide a whole new type of data to use for analytical validation.

- 3) The ability to perform controlled variations of key parameters in the wind tunnel has provided a unique set of data for validation, including blade airloads as a function of speed, thrust, and angle of attack. The data acquired during the dynamic stall sweeps should be especially valuable, helping to define the sensitivity of collective pitch (and thrust) to the onset and development of stall. Additionally, controlled slowed-rotor sweeps up to high advance ratio will be useful in understanding the aerodynamic and dynamic environment associated with this flight regime.
- 4) Initial comparisons between full-scale wind tunnel data and small-scale wind tunnel and flight data show many similarities but also some differences that are not yet understood. Additional analysis is required to determine if these differences are due to local aerodynamic effects of the wind tunnel walls or simply a difference in the quality of specific pressure measurements.

ACKNOWLEDGEMENTS

The authors gratefully acknowledge the significant efforts of the project partners (NASA, U.S. Army) as well as the U.S. Air Force, in the planning, preparation, and execution of this test. Special acknowledgement is made to Bob Kufeld, Alex Sheikman, and Doug Lillie (NASA), as well as Justin McLellan, Jonathan Gesek and the entire Air Force/Jacobs Engineering test team for making the test run as smoothly as it did. The Blade Displacement, RBOS, and PIV measurement teams deserve special recognition for their long-term commitment to technique development and data quality through this as well as previous test programs. Finally, the help and guidance of Wayne Johnson, Bill Bousman, and Bob Ormiston before, during, and after the test is gratefully acknowledged.

REFERENCES

1. Kufeld, R. M., Balough, D. L., Cross, J. L., Studebaker, K. F., Jennison, C. D., and Bousman, W. G., "Flight Testing of the UH-60A Airloads Aircraft," American Helicopter Society 50th Annual Forum, Washington D.C., May 1994.
2. Bousman, W. G., and Kufeld, R. M., "UH-60A Airloads Catalog," NASA TM-2005-212827, 2005.
3. Coleman, C. P. and Bousman, W. G., "Aerodynamic Limitations of the UH-60A Rotor," American Helicopter Society Aeromechanics Specialists' Conference, San Francisco, CA, January 1994.
4. Bousman, W. G., "A Qualitative Examination of Dynamic Stall from Flight Test Data," Journal of the American Helicopter Society, Vol. 43, (4), October 1998.
5. Potsdam, M., Yeo, H., and Johnson, W., "Rotor Airloads Prediction Using Loose Aerodynamic/Structural Coupling," American Helicopter Society 60th Annual Forum, Baltimore, MD, June 2004; Journal of Aircraft, Vol. 43, (3), May-June 2006.
6. Datta, A., Sitaraman, J., Chopra, I., and Baeder, J. D., "CFD/CSD Prediction of Rotor Vibratory Loads in High-Speed Flight," Journal of Aircraft, Vol. 43, (6), November-December 2006.
7. Lorber, P. F., "Aerodynamic Results of a Pressure-Instrumented Model Rotor Test at the DNW", Journal of the American Helicopter Society, Vol. 36, (4), October 1991.
8. Datta, A., Yeo, H., and Norman, T. R., "Experimental Investigation and Fundamental Understanding of a Slowed UH-60A Rotor at High Advance Ratios," American Helicopter Society 67th Annual Forum, Virginia Beach, VA, May 2011.
9. Romander, E., Norman, T. R., and Chang, I. C., "Correlating Coupled CFD Simulation with Wind Tunnel Test for the Full-Scale UH-60A Airloads Rotor," American Helicopter Society 67th Annual Forum, Virginia Beach, VA, May 2011.
10. Norman, T. R., Shinoda, P., Kitaplioglu, C., Jacklin, S. A., and Sheikman, A., "Low-Speed Wind Tunnel Investigation of a Full-Scale UH-60 Rotor System," American Helicopter Society 58th Annual Forum, Montreal, Canada, June 2002.
11. Norman, T. R., Theodore, C., Shinoda, P., Fuerst, D., Arnold, U. T. P., Makinen, S., Lorber, P., and O'Neill, J., "Full-Scale Wind Tunnel Test of a UH-60 Individual Blade Control System for Performance Improvement and Vibration, Loads, and Noise Control," American Helicopter Society 65th Annual Forum, Grapevine, TX, May 2009.
12. Buckanin, R. M., Gould, W., Losier, P. W., Downey, D. A., Lockwood, R., Webre, J. L., Hagan, J. F., Cason, R.

- W., and Youn, C. J., "Rotor Systems Evaluation, Phase I," AEFA Project No. 85-15, March 1988.
13. Hamade K., and Kufeld, R., "Modal Analysis of UH-60A Instrumented Rotor Blades," NASA TM 4239, November 1990.
 14. Gagnon, R., "Sub-Miniature Sensor Installation for UH-60A Main Rotor Blade Air Loads Flight Test Program," Presented at the International Telemetry Conference, 1989.
 15. Fletcher, J. W., and Tischler, M. B., "Improving Helicopter Flight Mechanics Models with Laser Measurements of Blade Flapping," American Helicopter Society 53rd Annual Forum, Virginia Beach, VA, May 1997.
 16. van Aken, J. and Yang, L., "Development of a New State-of-the-Art Data Acquisition System for the National Full-Scale Aerodynamics Complex Wind Tunnel," 47th AIAA Aerospace Sciences Meeting, Orlando, FL, January 2009.
 17. Olson, L. E., Barrows, D. A., Abrego, A. I., and Burner, A. W., "Blade Deflection Measurements of a Full-Scale UH-60A Rotor System," American Helicopter Society Aeromechanics Specialists Conference, San Francisco, CA, January 2010.
 18. Barrows, D. A., Olson L. E., Abrego, A. I., and Burner A. W., "Blade Displacement Measurements of an Airloads Full-Scale UH-60A Rotor System," 29th AIAA Applied Aerodynamics Conference, Honolulu, HI, June 2011.
 19. Meier, G. E. A., "Hintergrund Schlierenmeßverfahren," Deutsche Patentanmeldung DE 199 42 856 A1, 1999.
 20. Richard H., and Raffel M., "Principle and applications of the background oriented schlieren (BOS) method," Measurement Science and Technology (12), August 2001.
 21. Heineck, J. T., Schairer, E. T., Kushner, L. K., and Walker, L. A., "Retroreflective Background Oriented Schlieren (RBOS) as Applied to Full-Scale UH-60 Blade Tip Vortices," American Helicopter Society Aeromechanics Specialists Conference, San Francisco, CA, January 2010.
 22. Kushner, L. K. and Schairer, E. T., "Planning Image-Based Measurements in Wind Tunnels by Virtual Imaging," 49th AIAA Aerospace Sciences Meeting, AIAA 2011-930, Orlando, FL, January 2011.
 23. Johnson, W., "Technology Drivers in the Development of CAMRAD II," American Helicopter Society Aeromechanics Specialists Conference, San Francisco, CA, January 1994.
 24. Wadcock, A. J., Yamauchi, G. K., Solis, E., and Pete, A. E., "PIV Measurements in the Wake of a Full-Scale Rotor in Forward Flight," 29th AIAA Applied Aerodynamics Conference, Honolulu, HI, June 2011.
 25. Langer, H. J., Peterson, R. L., and Maier, T. H., "An Experimental Evaluation of Wind Tunnel Wall Correction Methods for Helicopter Performance," American Helicopter Society 52nd Annual Forum, Washington, D.C., June 1996.
 26. Theodore, C. R. and Tischler, M. B., "Development and Operation of an Automatic Rotor Trim Control System for the UH-60 Individual Blade Control (IBC) Wind Tunnel Test," American Helicopter Society Aeromechanics Specialists' Conference, San Francisco, CA, January 2010.
 27. Tung, C., Bousman, W. G., and Low, S., "A Comparison of Airload Data Between Model-Scale Rotor and Full-Scale Flight Test," American Helicopter Society Aeromechanics and Product Design, October 1995.
 28. Bousman, W. G., "A Note on Torsional Dynamic Scaling," Journal of the American Helicopter Society, Vol. 43, (2), April 1998.